

Anti-thixotropic dynamics in attractive colloidal dispersions: a shear restructuring driven by elastic stresses

Julien Bauland,¹ Gauthier Legrand,¹ Sébastien Manneville,^{1,2} Thibaut Divoux,¹ Arnaud Poulesquen,³ and Thomas Gibaud^{1, a)}

¹⁾Univ Lyon, Ens de Lyon, CNRS, Laboratoire de Physique, 69342 Lyon, France

²⁾Institut Universitaire de France (IUF)

³⁾ISEC, DPME, SEME, LFCM, Université of Montpellier, Marcoule, France

(Dated: 29 January 2025)

Due to rich rheological properties, dispersions of attractive colloidal particles are ubiquitous in industries. Specifically, upon experiencing a sudden reduction in shear rate, these dispersions may exhibit transient behaviors such as thixotropy—where viscosity increases over time—and anti-thixotropy, characterized by an initial viscosity decrease before reaching a steady state. While thixotropy has been described as a competition between structure buildup and disruption, the mechanisms of anti-thixotropy remain poorly understood. Here, we investigate the anti-thixotropic dynamics of carbon black particles dispersed in oil—a system known for exhibiting anti-thixotropy—through flow step-down experiments. Using a multi-technique approach combining rheology with velocimetry and structural characterizations, we show that viscosity decrease results from a decrease in wall slip concomitant to shear-induced structural rearrangements, indicating a transition from a dynamical network of fractal clusters into a network of loosely connected dense agglomerates. Additionally, after a characteristic anti-thixotropic time τ , a steady flow is reached. This time τ diverges with increasing shear rate at a critical value corresponding to a Mason number of one, indicating that anti-thixotropy occurs only when colloidal attraction outweighs viscous forces. More precisely, we show that the structural rearrangement underpinning the viscosity decrease is mediated by elastic stresses σ_e , such that $\tau \propto \sigma_e^{-3}$. Finally, on long time scales, the steady state is linked to a microstructure with nearly zero yield stress, indicating a loss of flow memory. These findings provide a mechanism for anti-thixotropy and suggest pathways for controlling viscosity and yield stress in attractive colloidal dispersions.

I. INTRODUCTION

Dispersions of attractive colloidal particles are non-Newtonian fluids commonly encountered in major industries, such as food and personal care products^{1,2}, construction materials³, and environmental sciences^{4,5}. Weak physical interactions between particles, such as Van der Waals forces, result in an attractive interaction potential with a strength similar to thermal energy. Beyond a critical particle volume fraction, attractive forces lead to the formation of a space-spanning network that imparts elastic, solid-like properties to the dispersions. At low particle volume fractions and strong attractions, such solids are referred to as colloidal gels⁶, characterized by a network with fractal-like organization.

Playing a key role in their functionality, colloidal gels exhibit dual behavior between a solid and a liquid, depending on the magnitude of shear forces relative to a critical threshold called the 'yield stress' σ_y ^{7–9}. When the applied stress exceeds the yield stress, colloidal gels exhibit a shear-induced solid-to-liquid transition referred to as 'yielding'^{10–12}. For 'reversible' gels, including carbon black gels¹³, clays^{14,15} and depletion gels¹⁶, this transition is fully reversible and the gel-state reform under rest. In such reversible gels, the versatility of their mechanical properties results from their dynamical microstructure, that can be reversibly modified by external stimulus. Consequently, a 'memory' of the flow can be encoded in the material, referring to its ability to retain structural or mechanical changes induced by external stimuli, even

after the stimuli are removed¹⁷. This ability arises because these materials exist in an out-of-equilibrium state with a complex energy landscape, scattered with multiple local minima. While some minima are inaccessible under normal thermal energy ($k_B T$), external stimuli such as shear provide the energy required to drive the gels into these otherwise unreachable states¹⁸. Memory is thus encoded by enabling transitions between configurations under the influence of external stimuli. Unlike colloidal glasses, whose dense packing restricts significant structural variation, the open structure of colloidal gels—due to their low volume fraction—allows for a wide range of distinct configurations. This structural diversity results in pronounced changes in mechanical properties, making memory effects particularly evident in colloidal gels. Notably, experimental studies have demonstrated the effect of shear on the rheological properties of attractive dispersions, showing that a 'rheological memory' of the flow history can be encoded under both continuous^{16,18–20} and oscillatory shear^{21,22}.

Irrespective of the nature of the flow, the effect of shear on the structure of attractive dispersions can be rationalized by the Mason number Mn ^{23,24}. This dimensionless number is defined as the ratio of the viscous drag force acting on particles (F_{visc}) to the attractive forces between two particles (F_{attr}), such that $Mn = \frac{F_{\text{visc}}}{F_{\text{attr}}} = \frac{6\pi\eta_f a^2 \dot{\gamma}}{U/\delta}$ with a (m) the particle radius, $\dot{\gamma}$ the shear rate, η_f the viscosity of the background fluid, and U (N.m) and δ (m) the depth and width of the attractive interaction potential, respectively. At high Mason numbers, i.e., $Mn \gg 1$, shear forces surpass attractive forces, causing particles to be fully dispersed and effectively erasing any previously encoded memory. In this limit, the system is fluid, and its viscosity is driven by hydrodynamic stresses

^{a)}Corresponding author, thomas.gibaud@ens-lyon.fr

σ_h . As the flow strength decreases and approaches $Mn = 1$, shear forces become comparable to attractive forces, resulting in microstructural rearrangements within the dispersion through which memory is encoded. At very low Mason numbers $Mn \ll 1$, shear forces are negligible, and the system behaves as an elastic solid^{25,26}. In this limit, the dispersion behaves as a solid, whose elasticity is driven by elastic stresses σ_e .

The interplay between shear forces and the microstructure at varying Mn leads to a finite timescale τ for the dispersion to adapt to a given flow strength and to reach a steady state. This adaptation results in transient dynamics, particularly pronounced when changing the flow rate from high to low Mn , where the system's response slows significantly. In this regime, two distinct transient phenomena have been identified: 'thixotropy' and 'anti-thixotropy'.

On the one hand, thixotropy^{23,27} refers to a continuous increase in viscosity following a flow step-down, i.e., a quick transition from high to low shear rates. From a microstructural point of view, thixotropy results from a competition between the structure build-up and destruction under shear, which is well captured by structural kinetics models²⁸. The thixotropic time τ_{thix} can be experimentally determined by so-called 'hysteresis loops', which involve applying a decreasing ramp of shear rate followed by an identical increasing ramp²⁹. Accordingly, the extent of thixotropy in a system can be determined from the Mnemosyne Number $My = \tau_{thix}\dot{\gamma}$, defined as the product of the thixotropic time and the imposed rate of deformation³⁰.

On the other hand, 'anti-thixotropy' is defined as a viscosity decrease following a flow step-down. Sometimes referred to as 'rheopexy'^{19,31} or 'negative thixotropy'³², anti-thixotropy has been reported for several attractive systems, where applying moderate shear rates typically leads to a viscosity decrease of an order of magnitude over extended timescales. These long transient dynamics have been attributed to the formation of dense agglomerates of particles that reduce the effective volume fraction of the dispersion, in comparison with fractal-like structures^{19,31,33–37}. More specifically, for carbon black dispersion in oil, Wang et al.³⁷ have shown that the long-lasting viscosity decay is associated with anti-thixotropy rather than a viscoelastic relaxation. Their measurements, based on orthogonal superposition, suggest that the structural densification underlying anti-thixotropy proceeds through interpenetration of fractal clusters. In the work of Hipp et al.³⁶, also carried on carbon black dispersions, the viscosity decay was rather attributed to an apparent behavior and the sedimentation of dense aggregates. Irrespective of the microstructural scenario, anti-thixotropy was also associated with a significant reduction of the yield stress, offering a means to tune the rheological properties of colloidal dispersion at will^{19,38}.

Yet, the specific microstructural scenario underlying the anti-thixotropic behavior in colloidal dispersions, as well as the physical mechanisms involved, remain to be clarified. In particular, what defines the upper shear rate limit of the thixotropic regime? What determines the duration of the transient regime needed to achieve a stationary state? Additionally, the potential contribution of heterogeneous flow profiles,

i.e., variations of the local shear rate in the sample such as wall slip and shear banding^{39–42}, must be investigated, as these phenomena are typically observed near the yield stress.

To address these issues, we conduct rheological experiments on attractive colloids, specifically carbon black particles (CB), dispersed in oil. The behavior of such dispersions is well-documented^{13,43,44}, making CB dispersion a reference system. These dispersions not only exhibit anti-thixotropy^{19,33,36,44–46} but also demonstrate delayed yielding^{47,48}, fatigue^{49,50}, rheo-conductive properties^{45,51}, sensitivity to flow cessations^{18,52}, and rheo-acoustic properties^{53,54}. Additionally, CB dispersions have practical applications in various fields, including rubber reinforcement^{55,56}, ink production⁵⁷, cement⁵⁸, and semi-solid flow batteries⁵⁹.

Using a multi-method approach, we couple rheometric tests with ultrasonic speckle velocimetry (USV) to measure local flow profiles, allowing us to distinguish between local and bulk contributions. To probe the hierarchical structure of CB dispersions and their connectivity in real time, we combine rheo-Ultra Small Angle X-ray Scattering (USAXS) and rheo-Electric Impedance Spectroscopy (EIS) measurements. First, USV reveals that the decrease in stress upon flow step-down is preceded by a wall-slip regime, during which the material organizes into a dynamic fractal network. Second, as shear propagates through the geometry gap, the fractal microstructure continuously rearranges into dense, large agglomerates, as confirmed by USAXS. Additionally, EIS shows that the dense and large agglomerates form a loosely connected dynamical network. The characteristic time τ of the anti-thixotropic response increases exponentially with the applied shear rate, up to a critical shear rate interpreted as a Mason number equal to one, where clusters become effectively sticky relative to shear forces. Finally, using flow cessation experiments, we show that the restructuring of the fractal structure as well the duration of the transient regime relies on elastic stresses that deform the partially connected fractal network. Interestingly, the steady state associated with the anti-thixotropic response results in a single structuring of the dispersions with a vanishingly small yield stress, indicating a lack of flow memory upon reaching steady state.

II. MATERIAL AND METHODS

A. Carbon black dispersions

Following refs.^{18,60}, CB particles (Vulcan[®]PF, Cabot, density $d_{cb} = 2.26 \pm 0.03$) are dispersed in mineral oil (RTM17 Mineral Oil Rotational Viscometer Standard, Paragon Scientific, viscosity $\eta_f = 252.1$ mPa.s at $T = 25^\circ\text{C}$, density $d_{oil} = 0.871$) at mass fractions c_w ranging from 4 to 10 % ($w \setminus w$). The corresponding volume fractions of CB particles ϕ_{r0} were calculated as $\phi_{r0} = c_w / [c_w + d_{cb}/d_{oil}(1 - c_w)]$. After mixing, dispersions are sonicated for 2 h in an ultrasonic bath (Ultrasonic cleaner, DK Sonic[®], United-Kingdom) to ensure that all particles are fully dispersed. We note that a mass fraction of 10 % $w \setminus w$ ($\phi_{r0} = 0.041$) constitutes an upper limit beyond which particles cannot be properly dispersed. Based

on TEM images and SAXS⁶⁰, Vulcan[®]PF particle are composed of nodules of radius $a \simeq 20$ nm that are fused together to form an aggregate of radius $r_0 \simeq 85$ nm with a fractal dimension $d_{fr_0} \simeq 2.8$. Vulcan PF particles are, therefore, small and compact aggregates in the spectrum of CB particles manufactured⁶¹. We specifically chose Vulcan[®] PF for its small particle size, which is well-suited for capturing large structures in SAXS. Additionally, we selected a relatively viscous mineral oil to slow sedimentation, ensuring that anti-thixotropic effects remain distinct from sedimentation effects (see VI- Sedimentation). The attraction potential of the CB particle is estimated⁶² to have a depth $U = 30 k_B T$ and a range $\delta = 0.7$ nm.

B. Rheology

Experiments were carried out with two stress-controlled rheometers: (i) a Haake RS6000 (Thermo Scientific) equipped with a coaxial cylinder geometry composed of two concentric polycarbonate cylinders (inner diameter 20 mm, outer diameter 22 mm, and height 40 mm), and (ii) an MCR 302 (Anton Paar) equipped with a parallel-plate geometry (diameter 50 mm, gap $e = 0.5$ mm). Additionally, stress jumps experiments were performed on a strain-controlled rheometer (ARES-G2, TA instruments) equipped with a cone-and-plate geometry (diameter 40 mm, cone angle 2° , truncation gap $47 \mu\text{m}$).

All rheological measurements were performed at $T = 25^\circ\text{C}$. After loading the CB dispersions, a preshear, $\dot{\gamma} = 500 \text{ s}^{-1}$ is first applied for 60 s to erase any shear history and fully rejuvenate the sample. Then, a flow step-down is applied from $\dot{\gamma} = 500 \text{ s}^{-1}$ to $\dot{\gamma}_0 \in [0.2, 100] \text{ s}^{-1}$ while measuring the resulting stress response $\sigma(t)$. The stress-controlled rheometers successfully imposed $\dot{\gamma}_0$ in about 0.8 s after the step flow, so data for $t \leq 0.8$ s are not considered (see Figure 10 in Appendix). As a result, the thixotropic response of CB dispersions reported at short time scales³⁷ is not investigated.

Finally, in addition to the flow step-down experiments, flow curves are performed by ramping down the shear rate from $\dot{\gamma} = 1000$ to 0.01 s^{-1} , using 10 points per decade with a duration $\Delta t = 1, 50$ and 100 s per point.

C. Ultrasonic speckle velocimetry (USV)

Velocity profiles are measured with ultrasound imaging using a homemade setup described in ref.⁶³. In brief, the local velocity $v(r, z, t)$ measured as a function of the position r in the gap, the vertical position z and time t . $v(r, z, t)$ is determined by cross-correlating successive ultrasonic speckle images of the dispersion. Hollow glass spheres with a mean diameter of $6 \mu\text{m}$ (SPHERICEL[®] 110P8, Potters Industries) were added to the dispersion ($\phi = 0.9\%$) to act as acoustic contrast agents. Two-dimensional velocity maps were obtained using an array of 128 piezoelectric transducers arranged along the vertical direction over 32 mm, covering about two-thirds of

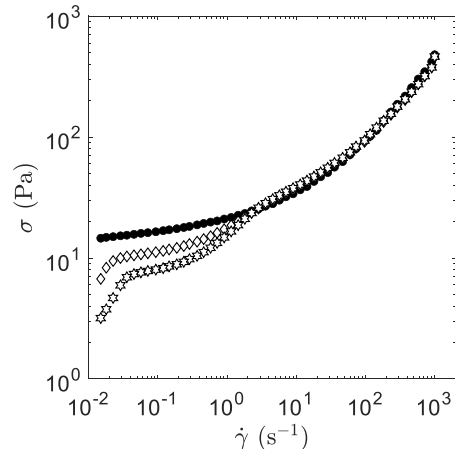


FIG. 1. Time-dependent apparent flow curves. Shear stress σ vs shear rate $\dot{\gamma}$ during flow sweep experiment on 3.2 % carbon black dispersion. Marker type codes for the shear duration at each shear rate: $\Delta t = 1$ (\bullet), 50 (\diamond), and 100 s (\star).

the height of the coaxial cylinder geometry. The velocity profiles are identical at given time in the vertical direction and are therefore averaged. Velocity maps $v(r, t)$ were acquired every 6 s for typically 2.10^3 s. To get statistically reliable data, the velocity maps were time-averaged over 100 successive cross-correlations.

D. Ultra Small Angle X-ray Scattering (USAXS)

The microstructural characteristics of the CB dispersion are probed using rheo-USAXS measurements conducted at the ID02 beamline within the European Synchrotron Radiation Facility (ESRF) in Grenoble, France⁶⁴. The incident X-ray beam, with a wavelength of 0.1 nm, is collimated to dimensions of $50 \mu\text{m}$ vertically and $100 \mu\text{m}$ horizontally. Utilizing an Eiger2 4M pixel array detector, two-dimensional scattering patterns are acquired. The subsequent data reduction process is detailed in^{65,66}. The scattering intensity $I(q)$ as function of the scattering wave vector q was derived by subtracting the two-dimensional scattering profiles of the CB dispersions and that of the mineral oil. Importantly, the resulting scattering intensity remained isotropic throughout this study and an azimuthal average was performed to obtain a one-dimensional spectrum $I(q)$. Measurements were conducted in both radial and tangential configurations, yielding similar results, showing the isotropic nature of the dispersions microstructure over the tested q range.

E. Electrical Impedance Spectroscopy (EIS)

Rheo-electrical measurements are performed using a stressed-controlled rheometer (MCR 302, Anton Par) equipped with a commercial set-up (Electro-Rheological De-

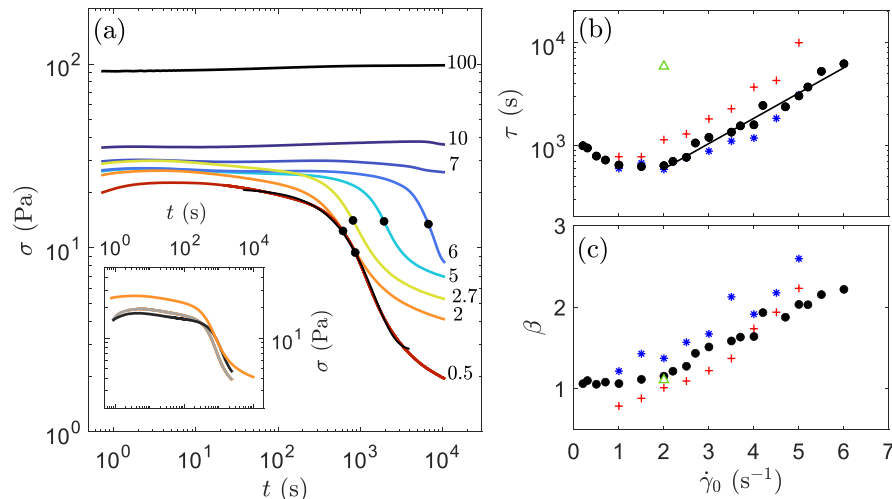


FIG. 2. Flow step-down experiments measured on the 3.2 % carbon black dispersion. (a) Stress response $\sigma(t)$ following a flow step-down from $\dot{\gamma} = 500 \text{ s}^{-1}$ to $\dot{\gamma}_0$. The values of $\dot{\gamma}_0$ are displayed on the right side. The black line is an example of fit by a compressed exponential decay $\sigma(t) = \sigma_0 + \sigma_1 \exp[-(t/\tau)^\beta]$, at low shear rates $\dot{\gamma}_0 < 7 \text{ s}^{-1}$. Black dots indicate $t = \tau$, the characteristic time of the compressed exponential decay. Inset displays σ vs. time t with $\dot{\gamma}_0 = 2 \text{ s}^{-1}$ in coaxial cylinder geometry (orange) and in parallel plate geometry with a gap size set at 0.25 and 2 mm (overlaid gray and black curves). (b) Characteristic time τ vs. shear rate $\dot{\gamma}_0$ for volume fractions of CB: $\phi = 4.1$ (*), 3.2 (\bullet), 2.4 (+) and 2 % (Δ). The black line is the best exponential fit for the 3.2 % data, following $\tau = \tau_0 \exp(\dot{\gamma}_0/\dot{\gamma}_1^*)$, with $\tau_0 = 193 \text{ s}$ and $\dot{\gamma}_1^* = 1.8 \text{ s}^{-1}$. (c) Exponent β of the compressed exponential model vs. $\dot{\gamma}_0$.

vice, Anton Paar) consisting of a conductive 50 mm parallel plate geometry. Electrical contact with the moving plate (rotor) is ensured by a liquid metal (Gallium-Indium eutectic 75.5 – 24.5% wt., ThermoFisher) to minimize solid friction⁴⁵. A variable voltage of magnitude 10 mV is applied at frequencies $f_e \in [2 - 5 \cdot 10^4]$ Hz using a potentiometer (SP-300 Potentiostat, Biologic). Frequency sweep allows for the measurement of the complex electrical impedance, $Z^*(f_e) = Z'(f_e) - iZ''(f_e)$, where Z' and Z'' stands for the real and imaginary part of Z^* , every 30 s during experiments lasting typically $2 \cdot 10^3$ s. A test at zero gap, i.e., when the two plates are in contact, shows that the set-up resistance is constant up to $f_e \leq 2 \cdot 10^3$ Hz, thus only data acquired in the range $f_e \in [2, 2 \cdot 10^3]$ Hz are considered for analysis.

III. RESULTS

A. Time-dependent flow properties at low shear rate

The CB dispersion at a volume fraction $\phi_{r0} = 3.2 \%$ displays a flow curve typical of yield stress fluids⁶⁰. As shown in Figure 1, focusing on the instantaneous flow curve (1 s/points starting from high shear), we observe that, at high shear rates, the dispersion flows, and the stress decreases with decreasing shear rate, reaching a plateau at low shear rates. The limit at zero shear rate indicates the dynamic yield stress, σ_y , which is the minimum stress required to initiate or sustain flow in a material that has already been deformed or is in motion. By increasing the measurement duration per point from 1 to 100 s, we observe that the flow curve remains identical at high

shear rates, which is not the case at low shear rates. Below $\dot{\gamma} \sim 1 \text{ s}^{-1}$, or for stresses near σ_y ³⁶, the apparent flow curve $\sigma(\dot{\gamma})$ is time-dependent. At a given shear rate, the stress decreases when the measurement duration increases. This behavior is consistent with anti-thixotropy but could also result from wall-slip^{39,42}. Furthermore, while flow curve measurements at varying rates offer a momentary view of the stress, they convolve time evolution with a continuous decrease of the shear rate. A more suitable protocol consists in conducting flow step-down experiments. These experiments involve switching from a high shear rate to a low shear rate as fast as possible, while monitoring the stress evolution over longer time. This experiment highlights the response of the material to a sudden change in shear rate, providing deeper and clearer insights into its dynamics.

B. Anti-thixotropic stress response during a flow step-down

We now focus on the bulk rheology of CB dispersions under flow step-down, i.e., from $\dot{\gamma} = 500 \text{ s}^{-1}$ down to a shear rate of interest $\dot{\gamma}_0$. Figure 2 shows the temporal evolution of the stress for the 3.2 % CB dispersion quenched to different shear rates $\dot{\gamma}_0 \in [100 - 0.5] \text{ s}^{-1}$. For $\dot{\gamma}_0 \geq 7 \text{ s}^{-1}$, we observe that a steady state is reached almost immediately, and the stress decreases by less than 10% over 10^4 s. In contrast, for $\dot{\gamma}_0 < 7 \text{ s}^{-1}$, the stress shows a delayed relaxation, i.e., it remains constant on short time scales and then decrease by a factor of 5 to 10 depending on the shear rate. The shape of the stress drop and the timescale over which it occurs are consistent with the anti-thixotropic response of CB dispersions,

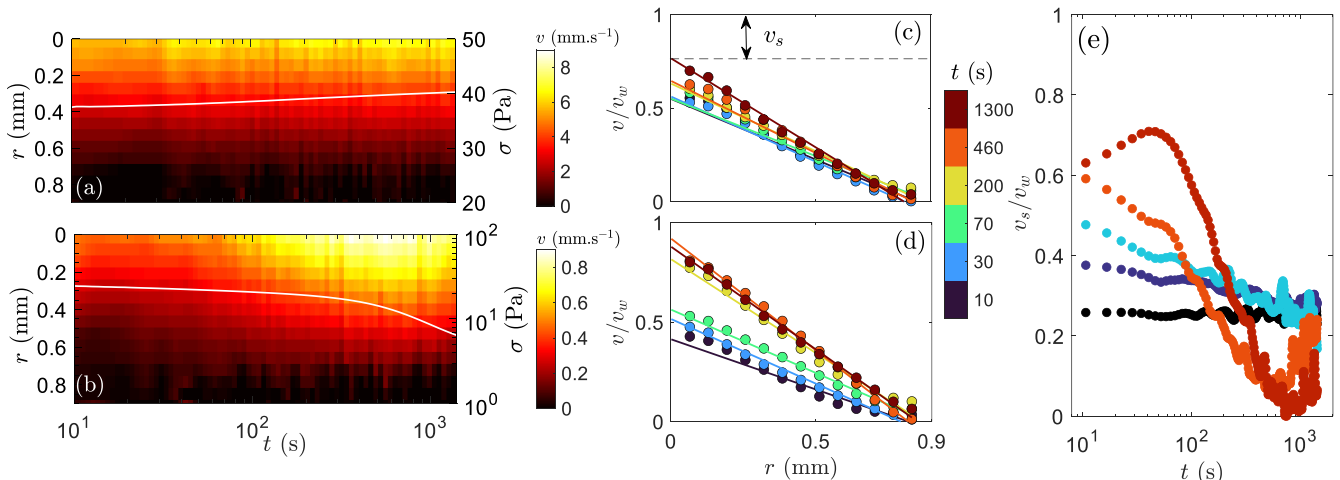


FIG. 3. Local velocity profiles measured on the 3.2 % carbon black dispersion using ultrasonic speckle velocimetry (USV) during flow step-down. (a)-(b) Spatiotemporal diagrams of the velocity data $v(r,t)$ as a function of position r and time t for (a) $\dot{\gamma}_0 = 10 \text{ s}^{-1}$, and (b) 1 s^{-1} . The stress response $\sigma(t)$ is displayed as a white line (right axis). (c)-(d) Corresponding velocity profiles measured at different times after imposing flow step-down of $\dot{\gamma}_0 = 10$ (c) and 1 s^{-1} (d). The fluid velocity v normalized by the wall velocity v_w is displayed as function of the radial distance in the gap r . Solid lines are the best linear fit of the data. (e) Time dependence of the wall slip velocity v_s , defined as the velocity difference between the rotor wall and the fluid $v_s = v_w - v_f$, normalized by the wall velocity. Colors code for the applied shear rate $\dot{\gamma}_0 = 100$ (black), 10 (blue), 5 (cyan), 1 (orange), and 0.5 s^{-1} (red).

as previously reported^{19,36,37}. It highlights the robustness of this behavior across different CB particles and apolar solvents. Additionally, this phenomenology is consistently observed in parallel plate geometry, and for various gap sizes (see inset in Fig. 2), ruling out any confinement or finite-size effect.

Our results point to a critical shear rate $\dot{\gamma}_0^* \approx 7 \text{ s}^{-1}$, which is robustly observed for various volume fractions of CB particles, $\phi_{r0} \in [2.4, 4.1] \%$ (see Fig. 11 in Appendix). Note the value of $\dot{\gamma}_0^*$ is consistent with the value previously reported for CB particles in mineral oil³⁷. Yet, $\dot{\gamma}_0^*$ depends on the nature of the solvent: a larger value of $\dot{\gamma}_0^* = 200 \text{ s}^{-1}$ was found when CB particles dispersed in propylene carbonate³⁶.

More quantitatively, the stress response $\sigma(t)$ associated with the anti-thixotropic behavior of the CB dispersions is well captured by a stretched exponential using the following expression: $\sigma = \sigma_0 + \sigma_1 \exp[-(t/\tau)^\beta]$, where σ_0 denotes the stress value when the shear rate is decreased, σ_1 is a stress scale, τ is a characteristic time, and β is an exponent controlling the shape of the exponential relaxation [see fit in Fig. 2(a)]. As shown in Figure 2(b), the time τ is roughly constant for $\dot{\gamma}_0 < 2 \text{ s}^{-1}$, and increases exponentially with the applied shear rate for $2 \leq \dot{\gamma}_0 \leq 6 \text{ s}^{-1}$. This dependence contrasts with the behavior of thixotropic timescales, which typically decrease with increasing shear rate²⁸. It also contrasts with the formation of log-rolling structures under confinement, where the time necessary to reach a steady state scales linearly with the applied shear rate^{62,67}. Moreover, while the critical shear rate $\dot{\gamma}_0^*$ appears independent of the volume fraction of primary CB particles ϕ_{r0} within the tested range, the anti-thixotropic time τ increases with a decrease of ϕ_{r0} for

a given shear rate [Fig. 2(b)]. Imposing $\dot{\gamma}_0 = 2 \text{ s}^{-1}$ yields $\tau = 640 \text{ s}$ for $\phi_{r0} = 3.2 \%$, and τ increases to 1140 s and 5900 s for $\phi_{r0} = 2.4$ and 2 %, respectively. Such an increase of τ with decreasing ϕ_{r0} has also been reported for dispersions of latex particles⁶⁸. The exponent β is positively correlated with τ and the exponential decay becomes more compressed ($\beta > 1$) when $\dot{\gamma}_0$ increases, yet without clear trend as a function of ϕ [Fig. 2(c)].

So far, we have shown that following a flow step-down, CB dispersions exhibit an anti-thixotropic drop in stress below a critical shear rate $\dot{\gamma}_0^* \approx 7 \text{ s}^{-1}$ that is independent of the tested volume fractions. The anti-thixotropic time τ increases exponentially with the applied shear rate, and also increases with the volume fraction. In the following sections, we focus on the 3.2 % CB dispersions and couple rheometric measurements to USV, USAXS, and EIS measurements to provide further insights on the microstructural scenario underpinning this macroscopic rheological response.

C. Flow velocity profiles

To investigate the potential contribution of heterogeneous flow to the macroscopic stress response evidenced in the previous section, we use USV to measure the local flow profile $v(r,t)$ a function of the position within the gap of the rheometer r and the time t just after a step flow-down over typically $2 \cdot 10^3 \text{ s}$. At a shear rate of $\dot{\gamma}_0 = 10 \text{ s}^{-1}$, both the stress and the flow profile are in a steady state [Fig. 3(b)]. In contrast, at a shear rate of $\dot{\gamma}_0 = 1 \text{ s}^{-1}$ where anti-thixotropy is observed, both the stress and the flow profile evolve over time

[Fig. 3(c)]. Figure 3(c)-(d) display typical examples of a velocity profiles, where the fluid velocity is plotted as a function of the radial distance r in the gap, measured at $\dot{\gamma}_0 = 10$ and 1 s^{-1} , respectively. All velocity profiles remain linear, i.e., no shear banding is observed. However, significant wall slip is observed at the rotor. The fluid velocity at the wall v_f is determined by a linear regression, and the degree of wall slip is then quantified by calculating the slip velocity defined as³⁹ $v_s = v_w - v_f$, where v_w is the (inner) wall velocity.

The normalized slip velocity v_s/v_w is displayed in Figure 3(e) against the time elapsed since the flow step-down. For all applied shear rates, the velocity profiles display some degree of slippage. For $\dot{\gamma}_0 = 100 \text{ s}^{-1}$, previously associated with a quasi-instantaneous steady-state based on the stress response, v_s/v_w is about 30 %. Second, the initial slip velocity measured at $t \approx 10 \text{ s}$ decreases for increasing $\dot{\gamma}_0$. For $\dot{\gamma}_0 = 1$ and 0.5 s^{-1} , v_s/v_w is as high as 60 % shortly after imposing $\dot{\gamma}_0$. For $\dot{\gamma}_0 = 100 \text{ s}^{-1}$, v_s/v_w is constant while at lower shear rates, v_s/v_w decreases over time and tends to about 30 %. For $\dot{\gamma}_0 = 0.5$ and 1 s^{-1} , v_s/v_w shows a non-monotonic evolution and goes through a minimum where $v_s = 0$, showing an absence of slip. The time corresponding to $v_s = 0$ nicely matches the anti-thixotropic time, with $\tau = 650$ and 850 s for $\dot{\gamma}_0 = 0.5$ and 1 s^{-1} , respectively. The correlation between the macroscopic stress decay and local velocity profiles at $\dot{\gamma}_0 = 1 \text{ s}^{-1}$ is further illustrated on the spatiotemporal diagram in Figure 3(b). The decrease of the stress σ starts when the fluid velocity approaches the wall velocity.

In summary, the slip velocity strongly correlates with the evolution of the shear stress. At low shear rates, specifically $\dot{\gamma}_0 = 0.5$ and 1 s^{-1} , the simultaneous decrease of the slip velocity v_s and the stress σ suggests that the material undergoes some structural reorganization under shear. In the following section, we investigate the microstructure of the CB dispersion under flow using USAXS and EIS.

D. Microstructure under shear

1. Rheo-X-ray scattering measurements

Rheo-USAXS experiments are performed to probe the microstructure of the 3.2 % CB dispersion over length scales ranging between 30 nm and 3 μm . We measure the 2D scattered intensity $I(q)$ as a function of the scattering wave vector q during flow step-down experiments. At these tested length scales, the scattering intensity $I(q)$ remains isotropic, with no sedimentation detected over the time scales examined (see Fig. 17 in Appendix).

Figure 4(a) displays Kratky plots of the 1D scattering intensity, i.e., $I.q^2$ vs. q , at various times under shear at $\dot{\gamma}_0 = 10 \text{ s}^{-1}$. The spectra reveal two to three structural length scales, depending on the shear rate, in agreement with previous works^{18,60}. During the rejuvenation step at 500 s^{-1} [indicated by black dotted lines in Fig. 4(a)], the structure of the dispersion shows two distinct peaks centered around $q \approx 7.10^{-2}$ and $q \approx 8.10^{-3} \text{ nm}^{-1}$. These peaks correspond to the form factor of the CB particles of size r_0 and to the

structuring of the CB particles into small fractal clusters of size ξ_{c_1} and fractal dimension d_{f_1} , respectively. After the flow step down, we observe the emergence of three length scales as observed by Koga et al.^{55,56} when CB particles are dispersed in a rubber matrix. This corresponds to the CB particles that aggregate into small clusters of size ξ_{c_1} and fractal dimension d_{f_1} inherited from the rejuvenation step that further aggregate into large clusters of size ξ_c and fractal dimension d_f .

When quenching to high shear rate such as $\dot{\gamma}_0 = 10 \text{ s}^{-1}$, the large cluster size quickly grows and then stabilizes at $q \approx 2.10^{-3} \text{ nm}^{-1}$ with no further changes observed in the scattering spectrum up to $t = 10^3 \text{ s}$. The same microstructure can be reproduced using a different shear protocol, namely a flow sweep, (see Fig. 14 in Appendix), demonstrating that for $\dot{\gamma} \geq 10 \text{ s}^{-1}$, the microstructure of the dispersion is unaffected by the flow history. In contrast, in the anti-thixotropic regime, at $\dot{\gamma} < 10 \text{ s}^{-1}$, the scenario is different. Indeed, the Kratky plot of the scattered intensity obtained when imposing $\dot{\gamma}_0 = 1 \text{ s}^{-1}$ shows a gradual increase of the large cluster size until $t \approx 30 \text{ s}$ [Fig. 4(b)]. Beyond this time, the low- q intensity scales as a power law $I \propto q^{-\alpha}$, indicating that the cluster size exceeds the detection range of the USAXS setup.

We now focus on the large-scale structures (sizes superior or equal to ξ_c) that are most affected in the anti-thixotropic regime. To capture the dynamics of structural changes, we use either a Guinier-Porod or a simple power-law model within the range $1.10^{-3} \leq q \leq 1.10^{-2} \text{ nm}^{-1}$, depending on which model best fits the data [see red curves in Fig. 4(a)-(b)]. The fitting parameters—the radius ξ_c for the Guinier-Porod and the power-law exponents α —are reported in Figure 4(c)-(d). For $\dot{\gamma}_0 = 0.5$ and 1 s^{-1} , the transition between the two models is highlighted by a dotted vertical line. At higher shear rates, i.e., $\dot{\gamma}_0 = 100$ and 10 s^{-1} , ξ_c increases for $t \approx 0.5$ and 3 s , respectively, and then remains constant as shown in Figure 4(a). It indicates a quick transition toward a steady state as hypothesized for such high shear rates. In contrast, for $\dot{\gamma}_0 = 0.5$ and 1 s^{-1} , ξ_c increases for $t \approx 10 \text{ s}$. From this time, data are best described by the power law model, with an exponent $\alpha = 2$, indicating the formation of a fractal-like network with a fractal dimension $d_f \approx 2$, and a mesh size beyond the USAXS detection range. Following this, the exponent α increases to 3.2, reflecting a continuous rearrangement of the network into a denser microstructure.

The power-law increase in intensity, with $\alpha > 3$, indicates that scattering is dominated by rough interfaces between the CB phases and the solvent. In this case, the fractal dimension of the interface d_{fs} can be determined using the relation $\alpha = 6 - d_{fs}$ ⁶⁹. Comparable exponent values have been observed in similar contexts, such as the anti-thixotropic response of CB particles in low viscosity solvent ($\alpha = 3.6$)³⁶, and CB dispersions exposed to high power ultra-sound ($\alpha = 3.7$)⁵⁴. These rough interfaces can be attributed to (i) micro-cracks forming within the CB network or (ii) the formation of large, dense agglomerates of CB particles. Supporting the second explanation, electron microscopy images of sheared polystyrene latex particle dispersions, which also display anti-thixotropy, show the formation of large agglomerates composed of densely packed particles⁶⁸. It suggests that the formation of dense ag-

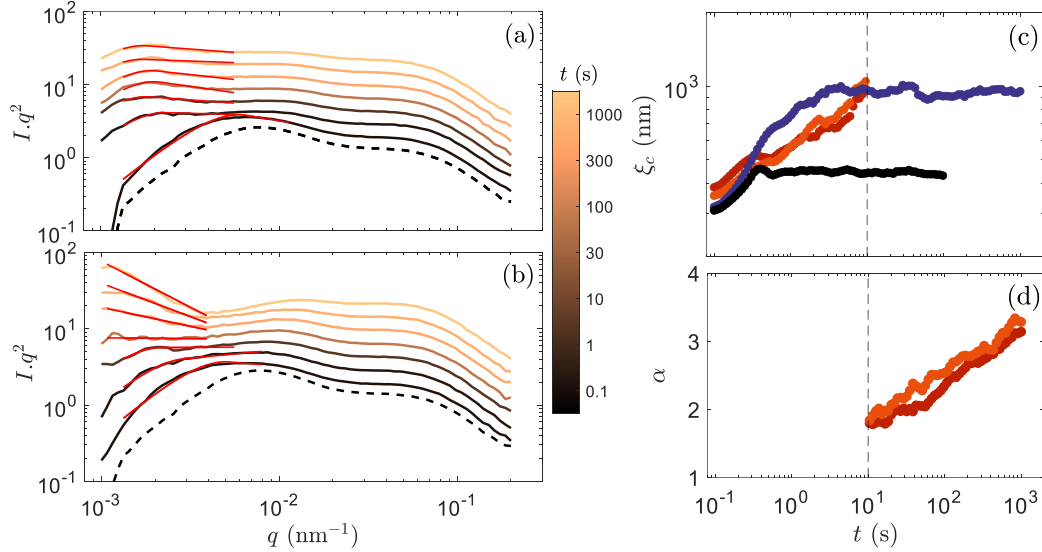


FIG. 4. Ultra-small angle X-ray scattering (USAXS) measurements conducted on the 3.2 % of carbon black (CB) dispersion during flow step-down. (a)-(b) Kratky plots $I.q^2$ vs. q of the scattering profiles acquired at different times after imposing a shear rate $\dot{\gamma}_0 = 10 \text{ s}^{-1}$ (a) and 1 s^{-1} (b). Black dotted curves are the scattering profile of the dispersion during the preshear step at $\dot{\gamma} = 500 \text{ s}^{-1}$. In (a)-(b), data are shifted along the y-axis for better visualization. (c)-(d) Quantitative analysis of the low- q region ($10^{-3} \leq q \leq 10^{-2} \text{ nm}^{-1}$) using either a Guinier-Porod or a simple power law model. The radius ξ_c of the Guinier-Porod or the power-law exponent α are shown as a function of time in panels (c) and (d), respectively, depending on which model best fits the data. Colors code for the applied shear rate $\dot{\gamma}_0 = 100$ (black), 10 (blue), 1 (orange) and 0.5 s^{-1} (red). Examples of fit are displayed as red lines in (a)-(b) panels.

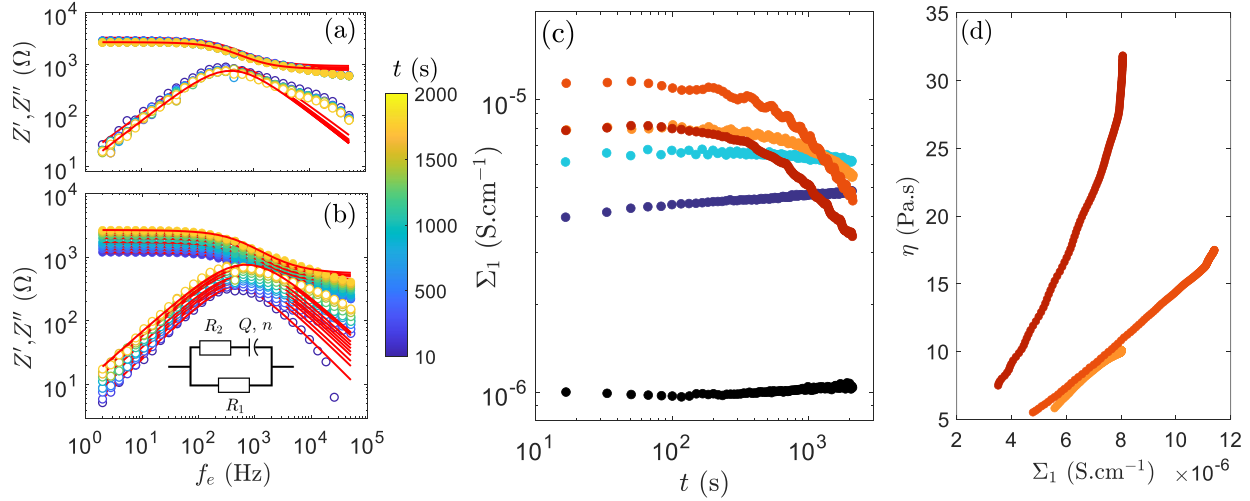


FIG. 5. Electrical impedance spectroscopy (EIS) measurements on a 3.2 % of carbon black (CB) dispersion during flow step-down. (a)-(b) Real part (Z') and imaginary part (Z'') of the complex impedance as a function of the input voltage frequency f_e measured at different times after stepping down the shear rate from 500 s^{-1} to $\dot{\gamma}_0 = 10 \text{ s}^{-1}$ (a) and 1 s^{-1} (b). Red curves are the best fits of the electrical model depicted in the inset of (b). (c) Temporal evolution of the conductivity Σ_1 associated with the structuring of carbon black particles. Colors code for the applied shear rate $\dot{\gamma}_0 = 100$ (black), 10 (blue), 5 (cyan), 2 (light orange), 1 (dark orange) and 0.5 s^{-1} (red). On the right panel, the same conductivity Σ_1 is displayed as a function of the time elapsed during the flow step-down. (d) Viscosity η vs. Σ_1 with identical color code.

glomerates in CB dispersions is more likely, which also aligns with previous hypothesis regarding the structure of CB dispersions, as determined by dielectric measurements³¹ and or-

thogonal superposition rheometry³⁷.

Finally, in Figure 4(c)-(d), the gradual evolution of ξ_c and α reflects a continuous structural building and rearrangement

within the sample during shear. This is consistent with USV measurements, which confirms that the dispersion does not exhibit plug flow, even at short times. For shear rates $\dot{\gamma}_0 = 0.5$ and 1 s^{-1} , the anti-thixotropic time τ roughly corresponds to the time when $\alpha = 3$, indicating that anti-thixotropy corresponds to a gradual restructuring of the dispersion, transitioning from fractal clusters to large, dense agglomerates. Considering the delay before the onset of anti-thixotropic stress decay, structural changes appear to have little effect on the measured stress or may be counterbalanced by the decrease in v_s , until $t \approx \tau$.

In conclusion, the steady-state flow at shear rates of $\dot{\gamma} = 100 \text{ s}^{-1}$ and 10 s^{-1} is characterized by a rapid evolution of the large cluster size. In contrast, the long-lasting transient regime observed during the anti-thixotropic response at $\dot{\gamma} = 0.5$ and 1 s^{-1} arises from the gradual transition from large fractal clusters into large and dense agglomerates which size exceed the range accessible using USAXS.

2. Rheo-Electrical impedance measurements

To further characterize the microstructure of the dispersion, we take advantage of the conductive properties of CB particles. We perform EIS measurements under shear by applying an alternating voltage of frequency f_e , and determining the complex impedance $Z^*(f_e)$ from the measured current. Figures 5(a)-(b) display the real $Z'(f_e)$ and imaginary $Z''(f_e)$ parts of Z^* measured at different times after imposing $\dot{\gamma}_0 = 10 \text{ s}^{-1}$ and 1 s^{-1} , respectively. The shape of $Z'(f_e)$ and $Z''(f_e)$ can be described by an electrical model composed of a resistance R_1 in parallel with a second resistance R_2 and a constant phase element of parameters Q and n^{70} [see inset in Fig. 5(b)]. In this model, R_1 is associated with the CB particles⁷¹, allowing us to calculate Σ_1 , the conductivity associated with the percolated network of CB particles (see Appendix for more details).

Figure 5(c) shows the temporal evolution of Σ_1 after applying $\dot{\gamma}_0 = 0.5, 1, 2, 5, 10,$ and 100 s^{-1} . At early times, i.e., $t < 100 \text{ s}$, the conductivity increases as the shear rate decreases, indicating a more connected microstructure at lower shear rates. For $\dot{\gamma}_0 = 100$ and 10 s^{-1} , the conductivity quickly reaches a quasi steady-state, indicating a rapid transition to equilibrium, as also seen in the rheometric and USAXS data. Specifically, for $\dot{\gamma}_0 = 100 \text{ s}^{-1}$, the low conductivity of the dispersion is consistent with isolated clusters within the dispersion. At low shear rates, namely $\dot{\gamma}_0 = 0.5, 1$ and 2 s^{-1} , the conductivity decreases with shearing time, corresponding to the decrease in stress measured by rheometry. This decrease in conductivity suggests the formation of denser but less connected agglomerates^{31,51}. For $\dot{\gamma}_0 = 5 \text{ s}^{-1}$, the conductivity only shows an initial decrease, when the maximum shear time measured by EIS is shorter than the anti-thixotropic time, $\tau = 3250 \text{ s}$. In Figure 5(d), the shear viscosity for $\dot{\gamma}_0 = 1$ and 2 s^{-1} , increases linearly with the conductivity, indicating that the structural rearrangements probed by dielectric measurements directly account for the evolution of the rheological properties. However, for $\dot{\gamma}_0 = 0.5 \text{ s}^{-1}$, the relationship

$\Sigma_1(\eta)$ is non-linear, possibly due to additional slip effects in the parallel-plate geometry.

In conclusion, consistent with USAXS data, EIS measurements confirm that anti-thixotropy arises from the reorganization of a homogeneous, well-connected structure into weakly connected and heterogeneous structures.

IV. DISCUSSION

A. Critical Mason number

We have observed anti-thixotropy in a CB dispersion at shear rates below a critical value $\dot{\gamma}_0^* \approx 7 \text{ s}^{-1}$. This phenomenology is robustly observed across the following volume fractions in CB particles: $\phi_{r_0} = 4.1, 3.2,$ and 2.4% . Similar critical shear rates have been reported in the literature and interpreted using the inverse of a Bingham number, $Bi^{-1} = \sigma/\sigma_y \simeq 1$, meaning that the instantaneous stress σ measured upon applying $\dot{\gamma}_0$ is close to the dynamic yield stress σ_y ³⁶. Applying this concept to our results, for a dispersion at $\phi_{r_0} = 3.2 \%$, the instantaneous stress measured before the onset of the anti-thixotropic response ranges between 20 and 30 Pa (Fig. 2), which approximately corresponds to a $Bi^{-1} \simeq 1$ when considering $\sigma_y = 14.7 \text{ Pa}$, as measured in the fast flow curve (Fig. 1).

To bring more insights to the physical understanding of $\dot{\gamma}_0^*$, we instead refer to the Mason number, $Mn = \frac{6\pi\eta_f a^2 \dot{\gamma}}{U\delta}$. For clusters of particles, the relevant length scale experiencing the drag force is not the CB particle itself but rather the cluster size $a = \xi_c$, estimated to be about $1.4 \mu\text{m}$ for the 3.2% dispersion at low shear rate⁶⁰. Assuming $\delta = 0.7 \text{ nm}$ and U comprised between 20 and $30 \text{ k}_B \text{ T}^{62}$, the critical Mason number $Mn^* \sim 1$ is reached for $\dot{\gamma} \in [11 - 20] \text{ s}^{-1}$, in fair agreement with the experimental value $\dot{\gamma}_0^* \approx 7 \text{ s}^{-1}$. Thus, $\dot{\gamma}_0^*$ is interpreted as a threshold where inter-cluster attraction forces are of the order of the shear forces.

In that framework, for applied shear rates $\dot{\gamma}_0 < \dot{\gamma}_0^*$, the clusters effectively behave as "sticky" particles and initially organize into a fractal network, as indicated by USAXS ($\alpha = 2$). Following an initial slip phase, likely due to a lubrication layer at the rotor wall, this fractal network progressively densifies, as evidenced by the increase in α and the decrease in conductivity measured by EIS. USV measurements further show that the anti-thixotropic time, τ , marks the end of wall slip, enabling better shear transmission through the gap, which eventually leads to a steady state.

B. Elastic stresses mediate the anti-thixotropic restructuring

For the initial network formed at $t = 0 \text{ s}$ to rearrange and densify, bonds must break, which likely involves straining the network and building up elastic stresses. Thus, the flow of CB suspensions below $\dot{\gamma}_0^*$ should be characterized by the emergence of an elastic contribution to the measured stress.

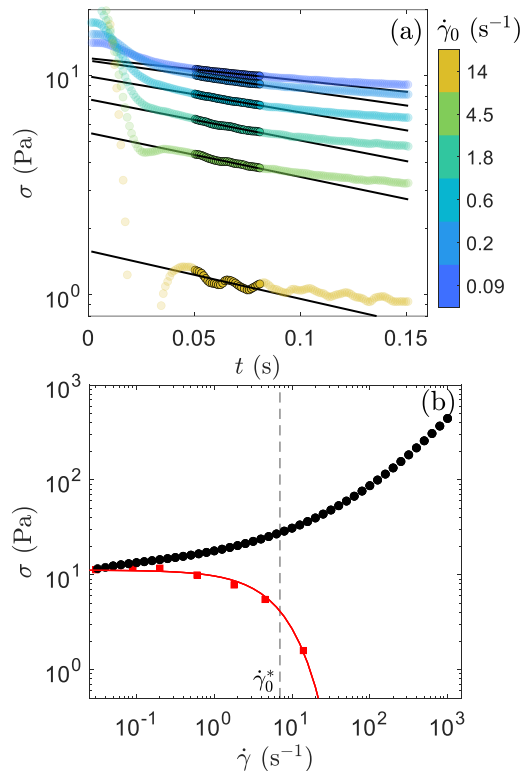


FIG. 6. Stress jump experiments and the measurements of the elastic stress σ_e for 3.2 % carbon black (CB) dispersion. (a) Stress relaxation measured at zero shear rate after applying different final shear rates. The black lines are the best exponential fits of the stress relaxation data between 5.10^{-2} and 8.10^{-2} s, which reads: $\sigma(t) = \sigma_e \exp(-t/t_e)$, with t_e and σ_e (see Table 6 in the Appendix) the slope and intercept in a semi-log plot. (b) Total (black circles) and elastic (red squares) stress measured during the flow curve of 3.2 % CB dispersion (see Fig. 1, rate: 1s/point). The red curve is the best fit of the elastic stress with the following function $\sigma_e = \sigma_y \exp(-\dot{\gamma}/\dot{\gamma}^*)$, with $\sigma_y = 12$ Pa and $\dot{\gamma}^* = 7 s^{-1}$.

To test this hypothesis, we conduct so-called "stress jump" experiments, previously used to separate viscous and elastic stress components in attractive colloidal dispersions^{72,73}. In this approach, the stress relaxation is measured immediately after flow cessation. Under shear, the total stress σ is assumed to be the sum of hydrodynamic and elastic contributions, i.e., $\sigma = \sigma_h + \sigma_e$. Upon flow cessation, the hydrodynamic stress component $\sigma_h \propto \eta \dot{\gamma}$ vanishes instantly as $\dot{\gamma} \rightarrow 0$, whereas the elastic stress, σ_e , requires a finite time to relax. Assuming that elastic stress relaxation initially follows an exponential decay, σ_e can be determined at $t = 0$, i.e., when the flow is stopped. Using this method and a strain-controlled rheometer, we performed a rapid flow sweep on the 3.2 % CB dispersion, stopping the flow at various shear rates. Figure 6(a) shows the stress relaxation measured during flow cessation for six different shear rates. The exponential fit of the data allows us to extract σ_e , which is reported in Figure 6(b) as a function of $\dot{\gamma}$, alongside the total stress measured during the flow sweep. For shear rates $\dot{\gamma} > 20 s^{-1}$, no elastic contribution was detected

($\sigma_e = 0$), consistent with the flow of isolated clusters governed by hydrodynamic forces⁶⁰. However, for $\dot{\gamma} \leq 20 s^{-1}$, the elastic contribution becomes significant, increasing to σ_y as the shear rate decreases.

The dependence of σ_e with $\dot{\gamma}$ follows an exponential decay: $\sigma_e = \sigma_y \exp(-\dot{\gamma}/\dot{\gamma}^*)$, with $\dot{\gamma}^* = 7 s^{-1}$ [see the red curve in Fig. 6(b)]. This shear rate, characterizing the emergence of elastic stresses during flow, is in excellent agreement with the critical shear rate $\dot{\gamma}_0^*$ below which anti-thixotropic behavior appears. This finding supports our hypothesis that the restructuring of the fractal network into large agglomerates relies on the elastic deformation of the CB network.

This interpretation is also consistent with a previous study on CB dispersions, where the orthogonal moduli G'_\perp and G''_\perp were measured using orthogonal superposition rheometry during the antithixotropic stress decrease³⁷. The authors reported a non-monotonic evolution of G'_\perp and G''_\perp , which initially increased and then decreased, while the shear stress consistently decreased. This difference in timescales between the decrease of these macroscopic variables was attributed to the buildup of structural anisotropy in the vorticity direction. In light of our results, the increase in G'_\perp and G''_\perp during antithixotropy could also be interpreted as an increase in the elastic contribution to the stress as the material undergoes shear densification. Furthermore, the peak in G'_\perp and G''_\perp roughly corresponds to the inflection point of the shear stress decrease and the anti-thixotropic time, supporting the idea that the material achieves maximum adhesion to the rotor at τ .

C. Scaling of the anti-thixotropic time

In light of the proposed mechanisms, the exponential increase of the anti-thixotropic time τ with the shear rate $\dot{\gamma}_0$ can be attributed to the fact that clusters become progressively less "sticky" as the shear rate increases. This leads to a longer time required for the system to form a percolated structure, which diverges as $\dot{\gamma}_0 \rightarrow \dot{\gamma}_0^*$ [Fig. 2(b)].

This phenomenology is likely a result of the step-flow shear protocol, where the shear rate is applied from high to low values. Indeed, previous studies have shown that the fluidization time for yield stress fluids decreases with increasing shear in creep experiments when starting from rest¹⁰⁻¹².

To further rationalize this dynamics, we compare the elastic stress σ_e (shown in Fig. 6), which decreases as $\dot{\gamma}_0^*$ is approached, with the anti-thixotropic time τ (shown in Fig. 2), which diverges near $\dot{\gamma}_0^*$. As shown in Fig. 7, σ_e and τ are correlated and follow the scaling relation $\tau^{1/3} = A/\sigma_e$, where $A = 80 Pa s^{1/3}$ is a constant. This scaling demonstrates that the amplitude of the elastic stress drives the dynamics of the anti-thixotropic restructuring. Given the difference in exponents between σ_e and τ , the value of τ is extremely sensitive to σ_e . This scaling also suggests the potential to define a dimensionless number for anti-thixotropy analogous to the Mnemosyne Number M_y used for thixotropy. However, evaluating such a number would require a broader dataset across different systems and concentrations, which is beyond the scope of this study.

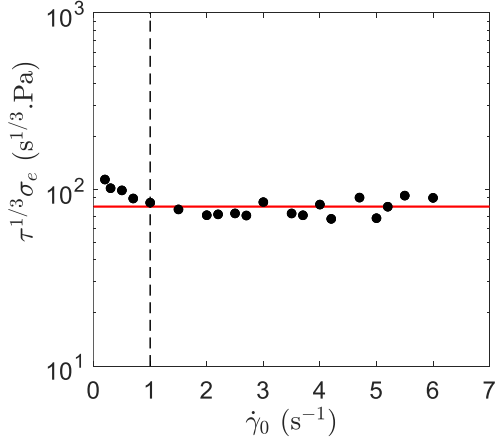


FIG. 7. Scaling relation between the anti-thixotropic time τ and the elastic stress σ_e as a function of the shear rate. At shear rates below 1 s^{-1} , indicated by the vertical dash line, slip at the rotor wall remains significant.

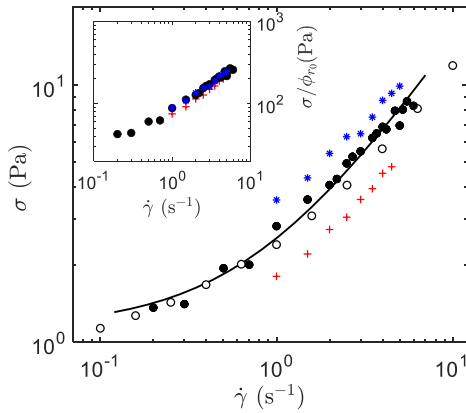


FIG. 8. Flow curves of carbon black (CB) dispersions with various volume fractions in the anti-thixotropic regime. Full markers are the final stress σ_∞ taken at $t = 10^4 \text{ s}$ after imposing a flow step-down, plotted as a function of the applied shear rate $\dot{\gamma}_0$ (denoted $\dot{\gamma}$ in x-axis for generality). Marker style and color codes for the volume fraction of CB $\phi_{r0} = 2.4 (+)$, $3.2 (\bullet)$, $4.1 (*)$. The black curve is the best fit of the 3.2% data with the Bingham model, yielding $\sigma_y = 1.2 \text{ Pa}$ and $\eta_{bg} = 1.4 \text{ Pa.s}$. Empty black markers are the flow curve of the 3.2% CB dispersion measured by flow sweep, after shearing the dispersion at $\dot{\gamma}_0 = 1 \text{ s}^{-1}$ during 10^4 s (see text for further details). Inset: stress normalized by the CB volume fraction versus the shear rate for $\phi_{r0} = 2.4 (+)$, $3.2 (\bullet)$, $4.1 (*)$.

D. Lack of memory upon reaching a steady state

After discussing the mechanisms behind the long-lasting dynamics of the anti-thixotropic stress response, we now focus on the steady state. To define this state, we arbitrarily use the stress value reached at $t = 10^4 \text{ s}$, which corresponds to $t \gg \tau$ [Fig. 2(a)], and denote it σ_∞ . This stress value is re-

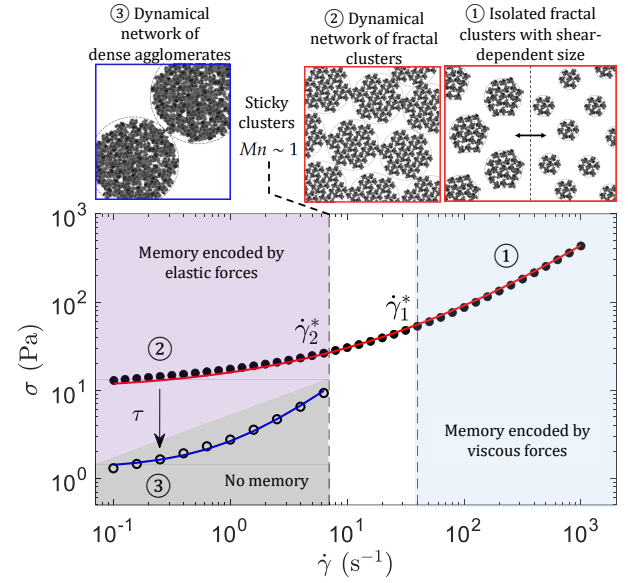


FIG. 9. Graphical summary of the flow properties of CB dispersions. Data corresponds to the dispersion with $\phi_{r0} = 3.2\%$: full black markers correspond to a flow sweep ($\Delta t = 1 \text{ s}$ per point) while empty markers correspond to the final stress values reached at $t = 10^4 \text{ s}$ following a step flow of shear rate for $\dot{\gamma}_0 < 7 \text{ s}^{-1}$. Red curve is the best fit with the three components model⁷⁵, which reads $\sigma = \sigma_y + \sigma_y(\dot{\gamma}/\dot{\gamma}^*)^{(1/2)} + \eta_{r0}\dot{\gamma}$, with $\sigma_y = 14.7 \text{ Pa}$, $\dot{\gamma}^* = 6.7 \text{ s}^{-1}$, $\eta_{r0} = 0.25 \text{ Pa.s}$. Blue curve is the best fit with the Bingham model, which reads $\sigma = \sigma_y + \eta_{bg}\dot{\gamma}$, with $\sigma_y = 1.2 \text{ Pa}$ and $\eta_{bg} = 1.4 \text{ Pa.s}$. ① The equilibrium size of fractal clusters is determined by the stress of the background fluid. ② The maximum clusters size is determined by their dynamic percolation at $\dot{\gamma}_1^*$ corresponding effective volume fraction in clusters $\phi_{eff} \simeq 0.4$. During a fast flow sweep, the yield stress value ($\sigma_y = 14.7 \text{ Pa}$) is inherited from the percolation point. ③ Below a second critical shear rate $\dot{\gamma}_2^*$ (denoted $\dot{\gamma}_0^*$ in the body text), where clusters become effectively sticky, dispersion exhibit anti-thixotropy corresponding to the transition from a network of fractal clusters to dense agglomerate within a characteristic time τ .

ported in Figure 8 against the applied shear rate $\dot{\gamma}_0$ (denoted $\dot{\gamma}$) to construct an effective flow curve. The effective flow curve is well described by a Bingham model, which is expressed as $\sigma = \sigma_y + \eta_{bg}\dot{\gamma}$, where the yield stress $\sigma_y = 1.2 \text{ Pa}$ is much lower than the value $\sigma_y = 14.7 \text{ Pa}$ measured from a rapid flow sweep (see Fig. 1). This suggests that the yield stress of the 3.2% CB dispersion can be tuned between 1.2 and 14.7 Pa, depending on the shear history. Specifically, if the flow step-down is interrupted by bringing the dispersion at rest ($\dot{\gamma} = 0$) at $t \ll \tau$, then $\sigma_y \simeq 14.7 \text{ Pa}$; if $t \gg \tau$, then $\sigma_y \simeq 1.2 \text{ Pa}$. Moreover, the Bingham model implies that the steady-state flow behavior of CB dispersions is characterized by a single viscosity, η_{bg} , across the range $\dot{\gamma} \in [0.1 - 10] \text{ s}^{-1}$. This indicates that the structure formed after the anti-thixotropic stress response—composed of dense, large agglomerates—remains stable over this range of shear rates. Indeed, if the agglomerate size varied along the flow curve, we would expect the viscosity η_{bg} to depend on the shear rate, $\eta_{bg} = \eta_{bg}(\dot{\gamma})$ ⁷⁴.

To test this hypothesis, we conducted a flow step-down at

$\dot{\gamma}_0 = 1 \text{ s}^{-1}$ for 10^4 s , as previously described, followed by a flow sweep between $0.1 \leq \dot{\gamma} \leq 10 \text{ s}^{-1}$. The result is shown in Figure 8, where the effective flow curve, built from the final stress values of the flow steps (black markers), and the actual flow curve (orange markers) overlap. This indicates that the anti-thixotropic behavior leads to a single structuring of the dispersions. This result is further supported by the final scattering curves at $t = 10^3 \text{ s}$, which are identical for $\dot{\gamma}_0 = 0.5$ and 1 s^{-1} , with $\alpha = 3.2$ [Fig. 4(d)]. Since the agglomerates are no longer fractal, we expect the viscosity of the dispersion to scale linearly with the volume fraction of primary CB particles ϕ_{r_0} . This is confirmed in the inset of Figure 8, where the effective flow curves can be rescaled by normalizing the stress σ_∞ by ϕ_{r_0} . These results support our hypothesis that the anti-thixotropic stress decay leads to a single structure, likely defined by a single agglomerate size. Consequently, at low shear rates, for $\dot{\gamma} < \dot{\gamma}_0^*$, the shear flow memory stems from the transient dynamics of the anti-thixotropic behavior.

Our results are reminiscent of the "flow-switched bistability" reported for attractive colloidal dispersions with non-interacting filler particles^{32,38}. In those studies, after a step-down in stress, it was observed that the presence of non-Brownian particles embedded in a gel matrix composed of attractive colloidal particles allowed the colloids to segregate into agglomerates under moderate shear stresses. This segregation led to the 'liquefaction' of the dispersion, characterized by a vanishingly small yield stress. Interestingly, the agglomerate or "blob" size was found to be independent of the applied stress, similar to our results when controlling the shear rate. This suggests a comparable mechanism in both cases. In Figure 2(b), we have shown that the anti-thixotropic time increases as the volume fraction of primary particles decreases. Based on this, it can be hypothesized that the effect of filler particles reported in^{32,38} is an excluded volume effect, concentrating the attractive colloidal particles. In other words, the addition of large non-interacting particles likely concentrates the attractive Brownian particles, bringing the anti-thixotropic time into measurable timescales. Consequently, anti-thixotropy may be an intrinsic property of sheared colloidal gels, with its characteristic timescale depending on the volume fraction of particles and, by extension, on the filler content.

V. CONCLUSION

In this study, we investigated the anti-thixotropic response of CB dispersions to flow step-down tests. Our results reveal that anti-thixotropy occurs below a critical shear rate of about $\dot{\gamma}_0^* \approx 7 \text{ s}^{-1}$. In this regime, following a flow step-down, the stress decays over a characteristic time τ and then reaches a steady state. Notably, τ increases exponentially with the applied shear rate.

Using a combination of Ultrasonic Speckle Velocimetry, Ultra Small Angle X-ray Scattering, and Electrical Impedance Spectroscopy measurements, we have shown that this behavior is driven by a combination of wall slip at short times, followed by slow structural rearrangements within the disper-

sion. Immediately after the flow step-down, fractal clusters of CB particles, formed during preshear, percolate into a dynamical fractal network. This network then undergoes further restructuring under shear, ultimately forming a dynamical network of weakly connected large and dense aggregates that are no longer fractal. In the anti-thixotropic regime, the driving force for this transition is the presence of elastic stress, such that the time τ required to reach the stationary anti-thixotropic state is inversely proportional to the elastic stress. More precisely, $\tau^{1/3} = A/\sigma_e$. Notably, the steady state reached after prolonged shear does not depend on the applied shear rate, suggesting that the dispersion retains no memory of the flow history. The critical shear rate $\dot{\gamma}_0^* \approx 7 \text{ s}^{-1}$, corresponding to a Mason number $Mn \simeq 1$, marks the threshold where clusters become effectively sticky and the emergence of an elastic contribution to the shear stress, enabling the deformation and the subsequent compaction of the microstructure. Our multi-method approach has provided a detailed microstructural scenario for the anti-thixotropic behavior in CB dispersions, paving the way for a deeper understanding of the structuring of colloidal dispersions under moderate shear.

Finally, we can provide a comprehensive overview of the shear-induced structuring of CB dispersions by combining the present work with our previous study⁶⁰. Figure 9 shows the flow curve of a 3.2% CB dispersion alongside a sketch of the microstructure evolution over four decades in shear rates. In sketch ①, the high shear rate region of the flow curve is characterized by a hydrodynamic regime, where the dispersion consists of isolated clusters. The equilibrium size of these clusters is directly influenced by the viscous forces⁶⁰. In this regime, steady-state is achieved rapidly (within a few seconds), and the flow memory is encoded by the hydrodynamic stresses σ_h of the background fluid. The characteristic shear rate $\dot{\gamma}_1^*$ marks the lower bound of this hydrodynamic regime, corresponding to the 'dynamic percolation' of fractal clusters, which determines their maximum size, as depicted in sketch ②. In the limit $\dot{\gamma} \rightarrow 0$, this fractal structure is conserved as long as the shear time or total strain remains low. However, below a second characteristic shear rate $\dot{\gamma}_2^*$ (denoted $\dot{\gamma}_0^*$ in the body text), the clusters become effectively sticky, and time-dependent effects, namely anti-thixotropy, emerge. Over time, the dispersion transitions from a dynamic network of fractal clusters —whose structure is inherited from $\dot{\gamma}_1^*$ — to large, dense agglomerates, as depicted in sketch ③. In this regime, flow memory is encoded by elastic stresses σ_e that deform and densify the fractal network ②, leading to a continuous decrease in viscosity and yield stress. Once a steady state is reached, the system no longer retains memory of the previous flow history, as a single structure is formed that is independent of the shear rates for $\dot{\gamma} < \dot{\gamma}_2^*$.

As a perspective, the structuring of attractive colloidal dispersions, controlled by flow rate and duration (Fig. 9), presents opportunities for exploitation. Rapidly quenching the flowing dispersion into a solid state through flow cessation could allow the formation of gels with varied structures and mechanical properties, without changing the formulation. These experiments could reveal how flow memory is imprinted in gels and find direct applications in injectable hy-

drogel or 3D printing processes.

AUTHOR CONTRIBUTIONS

JB, AP, and TG conducted the rheo-USAXS experiments. JB and SM performed the USV experiments. JB, TD, and GL carried out the Rheo-EIS experiments. Each author analyzed the data from their respective experiments. All authors contributed to data discussions and manuscript editing. JB and TG wrote the article. TG designed and supervised the project.

CONFLICTS OF INTEREST

There are no conflicts to declare.

ACKNOWLEDGEMENTS

The authors are especially grateful to the ESRF for beamtime at the beamline ID02 (proposal SC-5236) and Theyencheri Narayanan for the discussions and technical support during the USAXS measurements. This work was supported by the Région Auvergne-Rhône-Alpes "Pack Ambition Recherche", the LABEX iMUST (ANR-10-LABX-0064) of Université de Lyon, within the program "Investissements d'Avenir" (ANR-11-IDEX-0007), the ANR grants (ANR-18-CE06-0013 and ANR-21-CE06-0020-01) and European Union's Horizon Europe Framework Programme (HORIZON) under the Marie Skłodowska-Curie Grant Agreement 101120301. This work benefited from meetings within the French working group GDR CNRS 2019 "Solliciter LA Matière Molle" (SLAMM).

VI. APPENDIX

A. Rheological measurements

During flow step-down experiments, the stress-controlled rheometers successfully imposed $\dot{\gamma}_0$ in about 0.8 s. Consequently, data for $t \leq 0.8$ s are not considered, as evidenced in Figure 10. Additionally, flow step-down experiments were investigated at three volume fractions of CB particles, $\phi_{r_0} = 2.4, 3.2$ and 4.1 %. Figure 11(a)-(c) displays the complete data set, corresponding to Figure 2(b)-(c) in the main text.

B. Ultrasonic speckle velocimetry

Figure 12 displays the spatiotemporal diagrams of the velocity data for $\dot{\gamma}_0 = 100, 5$ and 0.5 s^{-1} .

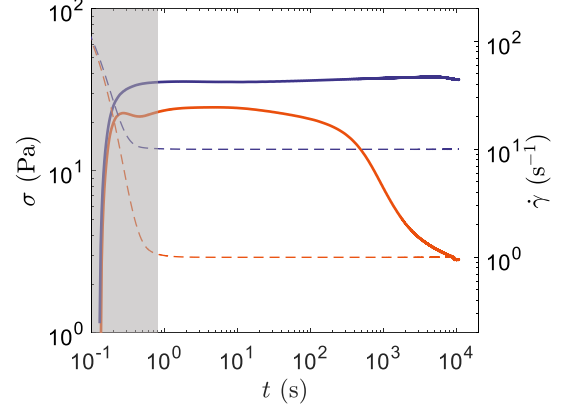


FIG. 10. Temporal evolution of the stress σ (solid lines) and shear rate $\dot{\gamma}$ (dotted lines) following a flow step-down from $\dot{\gamma} = 500$ s^{-1} to $\dot{\gamma}_0 = 10$ (blue) and 1 s^{-1} (orange). Data corresponds to a CB dispersion with a volume fractions $\phi_{r_0} = 3.2$ %.

C. Small angle X-ray scattering

Figures 13(a)-(b) display the evolution of the 1D scattering intensity $I(q)$ for the 3.2 % CB dispersion under application of $\dot{\gamma}_0 = 100$ and 0.5 s^{-1} .

To provide a quantitative analysis of the evolution of the low- q part of the spectrum, the intensity $I(q)$ in the range $10^{-3} \leq q \leq 10^{-2}$ nm^{-1} was adjusted by either a Guinier-Porod⁷⁶ (2) or a simple power-law model (3) depending on the shape of the data:

$$P(q) = \begin{cases} \frac{G}{q^s} \exp\left(\frac{-q^2 R_g^2}{3-s}\right) & q \leq q_1, \\ \frac{D}{q^m} & q \geq q_1 \end{cases} \quad (1)$$

$$P(q) = \frac{K}{q^\alpha} \quad (2)$$

Indeed, performing flow step-down leads to an increase of the cluster size that, for the lowest shear rates, exceeds the upper detection range of the USAXS set-up. Accordingly, the low- q structuring of the 3.2 % CB dispersion is sequentially captured by the Guinier-Porod and the power-law model (see Fig. 4 in the main text).

In Figure 14, we compare the scattering intensity of the 3.2 % dispersion measured at $\dot{\gamma} = 10$ and 100 s^{-1} under two different protocols: (i) a flow step-down (markers) and (ii) a flow sweep (solid lines). For both shear rates, data overlap, indicating that for $\dot{\gamma} > \dot{\gamma}_0^*$, the same steady state is achieved, regardless of the flow history.

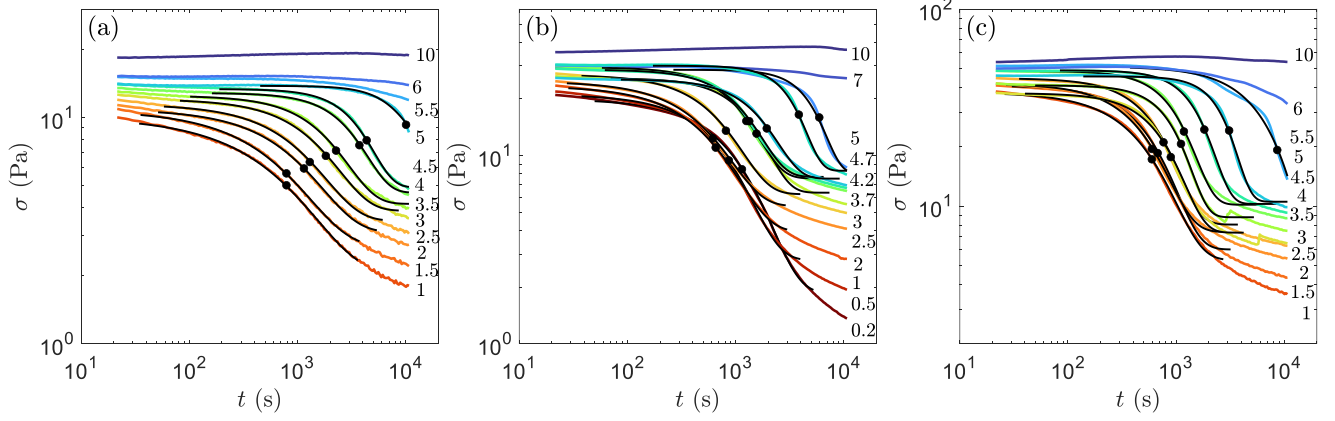


FIG. 11. Temporal evolution of the stress response σ following a flow step-down from $\dot{\gamma} = 500 \text{ s}^{-1}$ to $\dot{\gamma}_0$, for carbon black dispersions with volume fractions ϕ_{r0} of (a) 2.4, (b) 3.2 and (c) 4.1 %. The values of $\dot{\gamma}_0$ are displayed on the right side of each panel. Black lines are the best exponential fits $\sigma(t) = \sigma_0 + \sigma_1 \cdot \exp[-(t/\tau)^\beta]$, with $t = \tau$ indicated as a black dot.

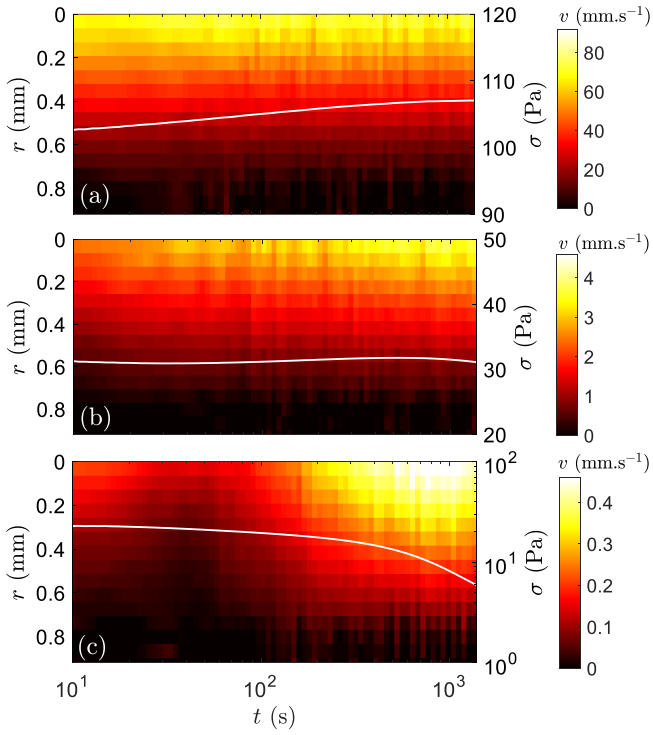


FIG. 12. Spatiotemporal diagrams of the velocity data $v(r,t)$ as a function of position r and time t for (a) $\dot{\gamma}_0 = 100 \text{ s}^{-1}$, (b) $\dot{\gamma}_0 = 5 \text{ s}^{-1}$ and (c) $\dot{\gamma}_0 = 0.5 \text{ s}^{-1}$. The stress response $\sigma(t)$ is displayed on the right vertical axis.

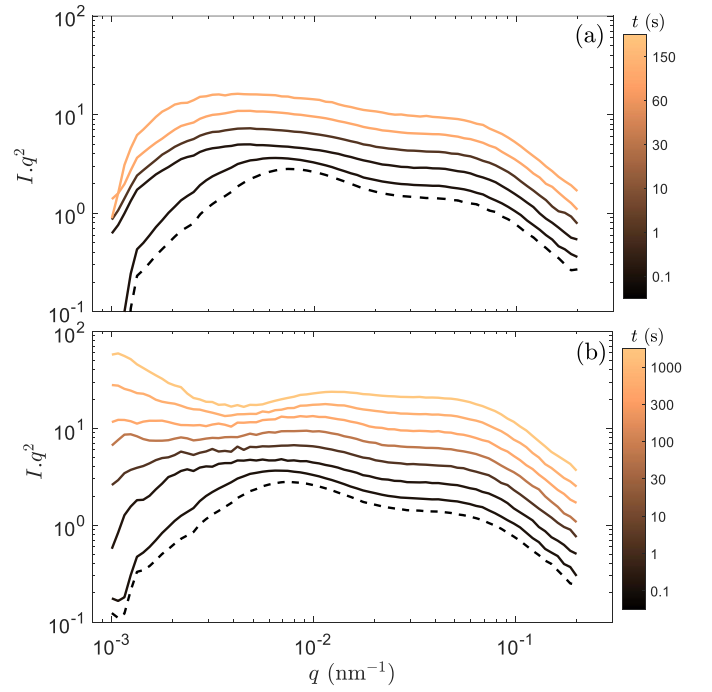


FIG. 13. Rheo-USAXS of the 3.2 % of carbon black (CB) dispersion during flow step-down. (a)-(b) Kratky plots $I \cdot q^2$ vs. q of the scattering profiles acquired at different times after imposing a shear rate of (a) $\dot{\gamma}_0 = 100 \text{ s}^{-1}$ and (b) and 0.5 s^{-1} . Black dotted curves are the scattering profile of the dispersion during the preshear step at $\dot{\gamma} = 500 \text{ s}^{-1}$.

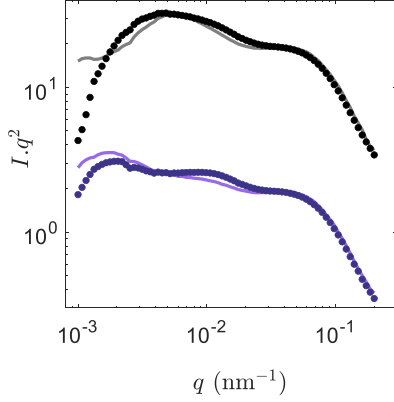


FIG. 14. Comparison of the scattering curves at $\dot{\gamma} = 10$ and 100 s^{-1} after a flow step-down from $\dot{\gamma} = 500 \text{ s}^{-1}$ to $\dot{\gamma}_0$ (markers) or a flow sweep with $\Delta t = 1 \text{ s}$ (solid lines).

D. Modeling of complex impedance

As determined from EIS measurements, the complex impedance $Z^*(f_e)$ is a function of the frequency f_e of the applied oscillatory tension. It can be captured by the following electrical model⁷¹ [see scheme in Fig. 5(b) of the main text]:

$$Z^*(f_e) = R_2 \frac{1 + R_2 Q (i2\pi f_e)^n}{1 + (R_1 + R_2) Q (i2\pi f_e)^n} \quad (3)$$

with a resistance R_1 in parallel with a second resistance R_2 and a constant phase element of parameters Q and n ⁷⁰. The constant phase element generalizes the behavior between a perfect capacitor ($n = 1$) and a resistance ($n = 0$). In this model, R_1 is associated with the resistance of CB particles, while R_2 and the constant phase element account for the ionic resistance of the solvent and the charge accumulation at the electrode surfaces, respectively⁷¹. Figure 15(a)-(c) displays the model parameters as a function of time and for different applied shear rates.

The resistance R_1 associated with the resistance of CB particles was converted into an electrical conductivity Σ_1 according $\Sigma_1 = k/R_1$, with $k = 0.013 \pm 0.005 \text{ cm}^{-1}$ the cell constant of the EIS set-up⁷¹.

E. Flow cessation experiments

To determine the elastic contribution to the shear stress, we perform flow cessation experiments or so-called "stress jump", and measured the relaxation of the stress as depicted in Figure 6(a) in the main text. We use a strain-controlled rheometer (ARES-G2, TA instruments), allowing to impose rapidly $\dot{\gamma} = 0 \text{ s}^{-1}$ in 40 ms, as depicted in Figure 16. Accordingly, the stress relaxation data were fitted with an exponential model in the range $5.10^{-2} \leq t \leq 8.10^{-2} \text{ s}$. The exponential

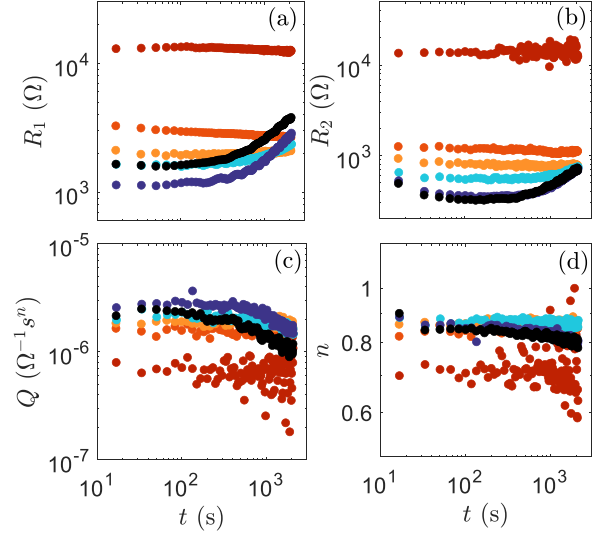


FIG. 15. Modeling of the complex impedance of the 3.2 % of carbon black (CB) dispersion using the electrical model displayed in inset of Figure 5(b), composed of a resistance R_1 in parallel with a second resistance R_2 and a constant phase element of parameters Q and n . Colors code for the applied shear rate $\dot{\gamma}_0 = 100$ (black), 10 (blue), 5 (cyan), 2 (light orange), 1 (dark orange) and 0.5 s^{-1} (red). Panels (a)-(d) display the temporal evolution of the model parameters during shear.

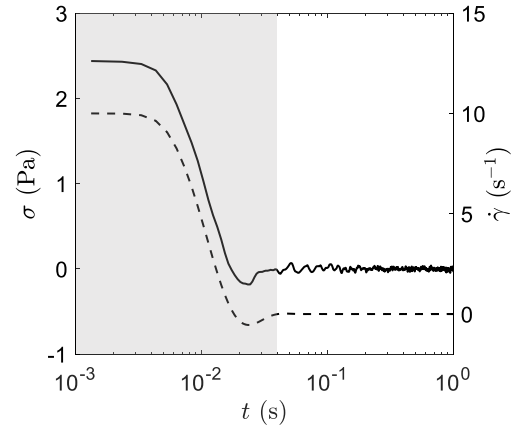


FIG. 16. Shear stress (solid line) and shear rate (dotted line) vs. time during flow cessation experiments performed on the background fluid (mineral oil) with a strain-controlled rheometer. From $\dot{\gamma} = 10 \text{ s}^{-1}$, the zero shear rate condition was imposed in about 40 ms.

model reads $\sigma(t) = \sigma_e \exp(-t/T)$, with T and σ_e the slope and intercept in a semi-log plot. The fit parameters are displayed in Table I for different shear rates.

$\dot{\gamma}$ (s ⁻¹)	σ_e (Pa)	t_e (s)
14	1.6	0.20
4.5	5.5	0.22
1.8	7.8	0.23
0.6	9.9	0.26
0.2	11.7	0.31
0.09	12	0.42
0.03	11.3	0.60
0.01	9.5	1

TABLE I. Parameters corresponding to the exponential fit of the stress relaxation data in Figure 6

F. Sedimentation

In a previous report, the anti-thixotropic behavior of CB dispersions was interpreted as an "apparent" behavior, resulting from the decrease of the hydrodynamic volume fraction of densifying agglomerates, and their concomitant sedimentation³⁶. Following the analysis of³⁶, the occurrence of sedimentation can be foreseen using the Shield number defined as the ratio of viscous (F_v) to gravitational (F_g) forces when considering sedimentation over the cluster size:

$$S = \frac{F_v}{F_g} = \frac{9\eta_f\dot{\gamma}}{2\xi_c g \Delta\rho} \quad (4)$$

with g the gravitational constant, ξ_c the characteristic cluster size, $\Delta\rho$ the difference of densities between cluster of particles and background fluid, η_f the viscosity of the background fluid.

The cluster density can be calculated from the internal volume fraction of CB particles in a cluster, $\phi_{int} = (\xi_c/r_0)^{(3-d_f)}$, with the cluster radius $\xi_c \approx 1.4 \mu\text{m}$, the fractal dimension $d_f = 2.5$ and the CB particle radius $r_0 = 85 \text{ nm}$ ⁶⁰. Then, the cluster density is given by $d_c = \phi_{int} \cdot d_{cb} + (1 - \phi_{int}) \cdot d_{oil} = 1.28 \cdot 10^3 \text{ kg} \cdot \text{m}^{-3}$. Taking, $\eta_f = 0.25 \text{ Pa} \cdot \text{s}$ and $g = 9.8 \text{ m} \cdot \text{s}^{-2}$, we found $S = 1$ for $\dot{\gamma} < 10^{-2} \text{ s}^{-1}$. It indicates that sedimentation is not likely to occur over the shear rates investigated. This assumption is supported by the scattered intensity associated with the CB particles length scale, $I(q > 7 \cdot 10^{-2} \text{ nm}^{-1}) = \phi_{r_0} \Delta\rho_{\text{slid}} V_{r_0}^2 P(q)$, that remains constant over $t = 2 \times 10^3 \text{ s}$, which is the longest acquisition time in USAXS (Figure 17). This indicates that the volume fraction of CB particles remains constant, ruling out sedimentation effects as an explanation for the initial stress decay with the characteristic time τ .

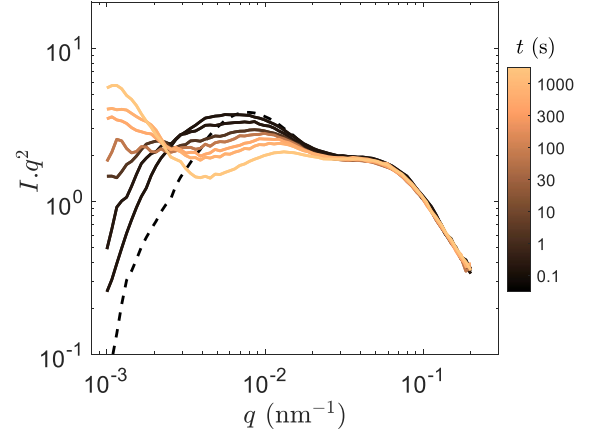


FIG. 17. Kratky plots $I \cdot q^2$ vs. q of the scattering profiles acquired at different times after imposing a shear rate of $\dot{\gamma}_0 = 1 \text{ s}^{-1}$ for the 3.2 % of CB dispersion. The black dotted curve is the scattering profile of the dispersion during the preshear step at $\dot{\gamma} = 500 \text{ s}^{-1}$. The intensity corresponding to the form factor of primary CB particles (at $q \approx 7 \cdot 10^{-2} \text{ nm}^{-1}$) remains constant during the anti-thixotropic stress decay, indicating that the volume fraction of CB particles ϕ_{r_0} remained constant over time.

- ¹T. Gibaud, N. Mahmoudi, J. Oberdisse, P. Lindner, J. S. Pedersen, C. L. Oliveira, A. Stradner, and P. Schurtenberger, "New routes to food gels and glasses," *Faraday Discuss.* **158**, 267–284 (2012).
- ²Y. Cao and R. Mezzenga, "Design principles of food gels," *Nat. Food* **1**, 106–118 (2020).
- ³A. Chougnat, T. Palermo, A. Audibert, and M. Moan, "Rheological behaviour of cement and silica suspensions: Particle aggregation modelling," *Cem. Concr. Res.* **38**, 1297–1301 (2008).
- ⁴K. Baskaran, M. Ali, K. Gingrich, D. L. Porter, S. Chong, B. J. Riley, C. W. Peak, S. E. Naleway, I. Zharov, and K. Carlson, "Sol-gel derived silica: A review of polymer-tailored properties for energy and environmental applications," *Microporous Mesoporous Mater.* **336**, 111874 (2022).
- ⁵S. Morariu, M. Teodorescu, and M. Bercea, "Rheological investigation of polymer/clay dispersions as potential drilling fluids," *J. Pet. Sci. Eng.* **210**, 110015 (2022).
- ⁶V. Trappe and P. Sandkühler, "Colloidal gels - Low-density disordered solid-like states," *Curr. Opin. Colloid Interface Sci.* **8**, 494–500 (2004).
- ⁷P. Coussot, "Yield stress fluid flows: A review of experimental data," (2014).
- ⁸D. Bonn, M. M. Denn, L. Berthier, T. Divoux, and S. Manneville, "Yield stress materials in soft condensed matter," *Rev. Mod. Phys.* **89**, 1–44 (2017), 1502.05281.
- ⁹A. Z. Nelson and R. H. Ewoldt, "Design of yield-stress fluids: A rheology-to-structure inverse problem," *Soft Matter* **13**, 7578–7594 (2017).
- ¹⁰T. Divoux, D. Tamarii, C. Barentin, and S. Manneville, "Transient shear banding in a simple yield stress fluid," *Phys. Rev. Lett.* **104** (2010).
- ¹¹T. Divoux, D. Tamarii, C. Barentin, S. Teitel, and S. Manneville, "Yielding dynamics of a Herschel-Bulkley fluid: A critical-like fluidization behaviour," *Soft Matter* **8**, 4151–4164 (2012).
- ¹²T. Gibaud, D. Frelat, and S. Manneville, "Heterogeneous yielding dynamics in a colloidal gel," *Soft Matter* **6**, 3482–3488 (2010).
- ¹³V. Trappe and D. A. Weitz, "Scaling of the viscoelasticity of weakly attractive particles," *Phys. Rev. Lett.* **85**, 449–452 (2000).
- ¹⁴F. Pignon, A. Magnin, and J.-M. Piau, "Butterfly light scattering pattern and rheology of a sheared thixotropic clay gel," *Physical Review Letters* **79**, 4689 (1997).
- ¹⁵N. A. Burger, B. Loppinet, A. Clarke, and G. Petekidis, "Tuning the mechanical properties of organophilic clay dispersions: Particle composition and preshear history effects," *Journal of Rheology* **68**, 695–707 (2024).
- ¹⁶N. Koumakis, E. Moghimi, R. Besseling, W. C. Poon, J. F. Brady, and G. Petekidis, "Tuning colloidal gels by shear," *Soft Matter* **11**, 4640–4648 (2015).
- ¹⁷T. Divoux, E. Agoritsas, S. Aime, C. Barentin, J.-L. Barrat, R. Benzi, L. Berthier, D. Bi, G. Biroli, D. Bonn, *et al.*, "Ductile-to-brittle transition and yielding in soft amorphous materials: perspectives and open questions," *Soft Matter* **20**, 6868–6888 (2024).
- ¹⁸N. Dages, L. V. Bouthier, L. Matthews, S. Manneville, T. Divoux, A. Poullesquen, and T. Gibaud, "Interpenetration of fractal clusters drives elasticity in colloidal gels formed upon flow cessation," *Soft Matter* **18**, 6645–6659 (2022).
- ¹⁹G. Ovarlez, L. Tocquer, F. Bertrand, and P. Coussot, "Rheopexy and tunable yield stress of carbon black suspensions," *Soft Matter* **9**, 5540–5549 (2013).
- ²⁰I. Sudreau, M. Auxois, M. Serval, É. Lécolier, S. Manneville, and T. Divoux, "Residual stresses and shear-induced overaging in boehmite gels," *Phys. Rev. Mater.* **6** (2022).
- ²¹E. Moghimi, A. R. Jacob, N. Koumakis, and G. Petekidis, "Colloidal gels tuned by oscillatory shear," *Soft Matter* **13**, 2371–2383 (2017).
- ²²M. Das and G. Petekidis, "Shear induced tuning and memory effects in colloidal gels of rods and spheres," *J. Chem. Phys.* **157** (2022).
- ²³J. Mewis and N. J. Wagner, "Thixotropy," *Adv. Colloid Interface Sci.* **147-148**, 214–227 (2009).
- ²⁴S. Jamali, R. C. Armstrong, and G. H. McKinley, "Time-rate-transformation framework for targeted assembly of short-range attractive colloidal suspensions," *Mater. Today Adv.* **5**, 100026 (2020).
- ²⁵J. Bauland, M. Leocmach, M. H. Famelart, and T. Croguennec, "Non-linear properties and yielding of enzymatic milk gels," *Soft Matter* **19** (2023), 10.1039/d2sm01556k.
- ²⁶Z. Varga and J. W. Swan, "Large scale anisotropies in sheared colloidal gels," *J. Rheol. (N. Y. N. Y.)* **62**, 405–418 (2018).
- ²⁷R. G. Larson and Y. Wei, "A review of thixotropy and its rheological modeling," *J. Rheol. (N. Y. N. Y.)* **63**, 477–501 (2019).
- ²⁸K. Dullaert and J. Mewis, "A structural kinetics model for thixotropy," *J. Nonnewton. Fluid Mech.* **139**, 21–30 (2006).
- ²⁹T. Divoux, V. Grenard, and S. Manneville, "Rheological hysteresis in soft glassy materials," *Phys. Rev. Lett.* **110**, 1–7 (2013).
- ³⁰S. Jamali and G. H. McKinley, "The Mnemosyne number and the rheology of remembrance," *J. Rheol. (N. Y. N. Y.)* **66**, 1027–1039 (2022).
- ³¹A. Narayanan, F. Mugele, and M. H. Duits, "Mechanical History Dependence in Carbon Black Suspensions for Flow Batteries: A Rheo-Impedance Study," *Langmuir* **33**, 1629–1638 (2017).
- ³²T. Larsen, J. R. Royer, F. H. Laidlaw, W. C. Poon, T. Larsen, S. J. Andreasen, and J. d. C. Christiansen, "Controlling the rheo-electric properties of graphite/carbon black suspensions by 'flow switching'," *Rheol. Acta* **63**, 283–289 (2024).
- ³³A. Medalia and E. Hagopian, "Rheology of dispersant-free aqueous slurries of carbon black," *Rheologica Acta* **3**, 100–111 (1963).
- ³⁴E. N'gouamba, M. Essadik, J. Goyon, T. Oerther, and P. Coussot, "Yielding and rheopexy of aqueous xanthan gum solutions," *Rheol. Acta* **60**, 653–660 (2021).
- ³⁵C. O. Osuji, C. Kim, and D. A. Weitz, "Shear thickening and scaling of the elastic modulus in a fractal colloidal system with attractive interactions," *Phys. Rev. E - Stat. Nonlinear, Soft Matter Phys.* **77** (2008).
- ³⁶J. B. Hipp, J. J. Richards, and N. J. Wagner, "Structure-property relationships of sheared carbon black suspensions determined by simultaneous rheological and neutron scattering measurements," *J. Rheol. (N. Y. N. Y.)* **63**, 423–436 (2019).
- ³⁷Y. Wang and R. H. Ewoldt, "New insights on carbon black suspension rheology – anisotropic thixotropy and anti-thixotropy," *J. Rheol. (N. Y. N. Y.)* **66**, 937–953 (2022), 2202.05772.
- ³⁸Y. Jiang, S. Makino, J. R. Royer, and W. C. Poon, "Flow-Switched Bistability in a Colloidal Gel with Non-Brownian Grains," *Phys. Rev. Lett.* **128** (2022).
- ³⁹T. Divoux, V. Lapeyre, V. Ravaine, and S. Manneville, "Wall slip across the jamming transition of soft thermoresponsive particles," *Phys. Rev. E - Stat. Nonlinear, Soft Matter Phys.* **92**, 1–6 (2015).
- ⁴⁰T. Gibaud, C. Barentin, and S. Manneville, "Influence of boundary conditions on yielding in a soft glassy material," *Phys. Rev. Lett.* **101** (2008).
- ⁴¹T. Gibaud, C. Perge, S. B. Lindström, N. Taberlet, and S. Manneville, "Soft Matter Multiple yielding processes in a colloidal gel under large amplitude oscillatory stress," *Soft Matter* **12**, 1701–1712 (2016).
- ⁴²R. H. Ewoldt, M. T. Johnston, and L. M. Caretta, "Experimental Challenges of Shear Rheology: How to Avoid Bad Data," *Complex fluids Biol. Syst. Exp. theory, Comput.* , 207–241 (2015).
- ⁴³T. Gibaud, T. Divoux, and S. Manneville, "Nonlinear Mechanics of Colloidal Gels: Creep, Fatigue, and Shear-Induced Yielding," in *Encycl. Complex. Syst. Sci.* (Springer Berlin Heidelberg, 2020) pp. 1–24.
- ⁴⁴J. J. Richards, P. Z. Ramos, and Q. Liu, "A review of the shear rheology of carbon black suspensions," *Front. Phys.* , 1–11 (2023).
- ⁴⁵A. Helal, T. Divoux, and G. H. McKinley, "Simultaneous Rheoelectric Measurements of Strongly Conductive Complex Fluids," *Phys. Rev. Appl.* **6** (2016).
- ⁴⁶Y. Wang and R. H. Ewoldt, "New insights on carbon black suspension rheology—Anisotropic thixotropy and antithixotropy," *J. Rheol. (N. Y. N. Y.)* **66**, 937–953 (2022).
- ⁴⁷T. Gibaud, D. Frelat, and S. Manneville, "Heterogeneous yielding dynamics in a colloidal gel," *Soft Matter* **6**, 3482–3488 (2010).
- ⁴⁸V. Grenard, T. Divoux, N. Taberlet, and S. Manneville, "Timescales in creep and yielding of attractive gels," *Soft matter* **10**, 1555–1571 (2014).
- ⁴⁹T. Gibaud, C. Perge, S. B. Lindström, N. Taberlet, and S. Manneville, "Multiple yielding processes in a colloidal gel under large amplitude oscillatory stress," *Soft Matter* **12**, 1701–1712 (2016).
- ⁵⁰C. Perge, N. Taberlet, T. Gibaud, and S. Manneville, "Time dependence in large amplitude oscillatory shear: A rheo-ultrasonic study of fatigue dynamics in a colloidal gel," *Journal of Rheology* **58**, 1331–1357 (2014).
- ⁵¹J. J. Richards, J. B. Hipp, J. K. Riley, N. J. Wagner, and P. D. Butler, "Clustering and Percolation in Suspensions of Carbon Black," *Langmuir* **33**, 12260–12266 (2017).
- ⁵²L.-V. Bouthier and T. Gibaud, "Three length scales colloidal gels: the clusters of clusters versus the interpenetrating clusters approach," *J. Rheol. (N.*

- Y. N. Y). **67**, 621–633 (2023).
- ⁵³T. Gibaud, N. Dagès, P. Lidon, G. Jung, L. C. Houré, M. Sztucki, A. Poulesquen, N. Hengl, F. Pignon, and S. Manneville, “Rheoacoustic Gels: Tuning Mechanical and Flow Properties of Colloidal Gels with Ultrasonic Vibrations,” *Physical Review X* **10**, 1–21 (2020), 011028, 1905.07282.
- ⁵⁴N. Dagès, P. Lidon, G. Jung, F. Pignon, S. Manneville, and T. Gibaud, “Mechanics and structure of carbon black gels under high-power ultrasound,” *J. Rheol. (N. Y. N. Y.)* **65**, 477–490 (2021).
- ⁵⁵T. Koga, M. Takenaka, K. Aizawa, M. Nakamura, and T. Hashimoto, “Structure factors of dispersible units of carbon black filler in rubbers,” *Langmuir* **21**, 11409–11413 (2005).
- ⁵⁶T. Koga, T. Hashimoto, M. Takenaka, K. Aizawa, N. Amino, M. Nakamura, D. Yamaguchi, and S. Koizumi, “New insight into hierarchical structures of carbon black dispersed in polymer matrices: A combined small-angle scattering study,” *Macromolecules* **41**, 453–464 (2008).
- ⁵⁷L. Liu, Z. Shen, X. Zhang, and H. Ma, “Highly conductive graphene/carbon black screen printing inks for flexible electronics,” *Journal of colloid and interface science* **582**, 12–21 (2021).
- ⁵⁸H. Li, H.-g. Xiao, and J.-p. Ou, “Effect of compressive strain on electrical resistivity of carbon black-filled cement-based composites,” *Cement and Concrete Composites* **28**, 824–828 (2006).
- ⁵⁹Q. Liu and J. J. Richards, “Rheo-electric measurements of carbon black suspensions containing polyvinylidene difluoride in N-methyl-2-pyrrolidone,” *J. Rheol. (N. Y. N. Y.)* **67**, 647–659 (2023).
- ⁶⁰J. Bauland, L.-V. Bouthier, A. Poulesquen, and T. Gibaud, “Attractive carbon black dispersions: Structural and mechanical responses to shear,” *J. Rheol.* **68**, 429–443 (2024).
- ⁶¹R. Fernandez Martinez, M. Iturrondobetia, J. Ibarretxe, and T. Guraya, “Methodology to classify the shape of reinforcement fillers: optimization, evaluation, comparison, and selection of models,” *Journal of Materials Science* **52**, 569–580 (2017).
- ⁶²Z. Varga, V. Grenard, S. Pecorario, N. Taberlet, V. Dolique, S. Manneville, T. Divoux, G. H. McKinley, and J. W. Swan, “Hydrodynamics control shear-induced pattern formation in attractive suspensions,” *Proc. Natl. Acad. Sci. U. S. A.* **116**, 12193–12198 (2019).
- ⁶³T. Gallot, C. Perge, V. Grenard, M. A. Fardin, N. Taberlet, and S. Manneville, “Ultrafast ultrasonic imaging coupled to rheometry: Principle and illustration,” *Rev. Sci. Instrum.* **84**, 20–22 (2013).
- ⁶⁴T. Narayanan, R. Dattani, J. Möller, and P. Kwaśniewski, “A microvolume shear cell for combined rheology and x-ray scattering experiments,” *Review of Scientific Instruments* **91** (2020).
- ⁶⁵P. Panine, M. Gradzielski, and T. Narayanan, “Combined rheometry and small-angle x-ray scattering,” *Review of Scientific Instruments* **74**, 2451–2455 (2003).
- ⁶⁶T. Narayanan, M. Sztucki, T. Zinn, J. Kieffer, A. Homs-Puron, J. Gorini, P. Van Vaerenbergh, and P. Boesecke, “Performance of the time-resolved ultra-small-angle X-ray scattering beamline with the Extremely Brilliant Source,” *J. Appl. Crystallogr.* **55**, 98–111 (2022).
- ⁶⁷V. Narayanan, N. Taberlet, and S. Manneville, “Shear-induced structuration of confined carbon black gels: Steady-state features of vorticity-aligned flocs,” *Soft Matter* **7**, 3920–3928 (2011).
- ⁶⁸P. D. Mills, J. W. Goodwin, and B. W. Grover, “Shear field modification of strongly flocculated suspensions - Aggregate morphology,” *Colloid Polym. Sci.* **269**, 949–963 (1991).
- ⁶⁹G. Beaucage and D. W. Schaefer, “Structural studies of complex systems using small-angle scattering: a unified Guinier/power-law approach,” *J. Non. Cryst. Solids* **172-174**, 797–805 (1994).
- ⁷⁰K. S. Cole, “Electric impedance of suspensions of spheres,” *J. Gen. Physiol.* **12**, 29–36 (1928).
- ⁷¹G. Legrand, S. Manneville, G. H. McKinley, and T. Divoux, “Dual origin of viscoelasticity in polymer-carbon black hydrogels: a rheometry and electrical spectroscopy study,” (2022).
- ⁷²K. Dullaert and J. Mewis, “Thixotropy: Build-up and breakdown curves during flow,” *J. Rheol. (N. Y. N. Y.)* **49**, 1213–1230 (2005).
- ⁷³R. Massaro, G. Colombo, P. Van Puyvelde, and J. Vermant, “Viscoelastic cluster densification in sheared colloidal gels,” *Soft Matter* **16**, 2437–2447 (2020).
- ⁷⁴G. Wang, A. M. Fiore, and J. W. Swan, “On the viscosity of adhesive hard sphere dispersions: Critical scaling and the role of rigid contacts,” *Journal of Rheology* **63**, 229–245 (2019).
- ⁷⁵M. Caggioni, V. Trappe, and P. T. Spicer, “Variations of the Herschel–Bulkley exponent reflecting contributions of the viscous continuous phase to the shear rate-dependent stress of soft glassy materials,” *J. Rheol. (N. Y. N. Y.)* **64**, 413–422 (2020).
- ⁷⁶B. Hammouda, “A new Guinier-Porod model,” *J. Appl. Crystallogr.* **43**, 716–719 (2010).